博士学位論文

Cluster formation in neutron-rich Be and B isotopes
（中性子過剰な Be と B 同位体におけるクラスター形成）

Hideaki MOTOKI
本木　英陽

北海道大学大学院理学院
宇宙理学専攻
原子核理論研究室

２０２３年３月

Abstract

This dissertation is based on [1]: (H. Motoki, Y. Suzuki, T. Kawai, and M. Kimura, Progress of Theoretical and Experimental Physics **2022**(11), 113D01 (2022)).

Background:
Recently, experiments performed using the $(p, p\alpha)$ reactions have revealed a negative correlation between the α cluster formation and neutron number in Sn isotopes, showing a trend opposite to that predicted theoretically in Be and B isotopes. Although the observed charge radii of the Be and B isotopes suggest the formation of clusters as the neutron drip-line is approached, these radii themselves are not a physical quantity that can directly probe the cluster structure.

Purpose:
I directly investigate the cluster formation in Be and B isotopes as the neutron drip-line is approached to elucidate the effect of excess neutrons for the possibilities of ^{6}He and ^{8}He clustering as well as α clustering.

Method:
All nuclei are described by antisymmetrized molecular dynamics (AMD) plus generator coordinate method (GCM) framework. The cluster formations are directly analyzed by the spectroscopic factors (S-factor) of ^{6}He and ^{8}He clusters as well as α clusters using the Laplace expansion method.

Results:
Sum of the S-factors, i.e. $S(\alpha)$, $S(^6\text{He})$, and $S(^8\text{He})$, increases as the neutron drip-line approaches although $S(\alpha)$ decreases. This behavior might be correlated with the enhancement of clustering which is analyzed by the intrinsic proton density distributions.

Conclusions:
The results indicate that the excess neutrons contribute to yield ^{6}He and ^{8}He clusters as well as α clusters. The decrease in $S(\alpha)$ toward the neutron drip-line in Be and B isotopes is due to considering only the ground state of the residual nuclei, meaning that it does not indicate that α cluster formation is not increased. Thus, $S(\alpha)$ is not enough to estimate the enhancement of clustering in Be and B isotopes.

Contents

1 Introduction

1.1 Clustering phenomena in nuclei

An atomic nucleus is a finite quantum many-body system composed of nucleons (protons and neutrons) that strongly interact with each other governed by the nuclear force. This finite nucleus is an isolated system and therefore has a degree of freedom related to space inversion and rotation different from the infinite nuclear matter. The nucleus has not only an energetically stable ground state but also excited states which have higher energies and decay after specific lifetime. The nuclear force between nucleons is a strong attraction that greatly exceeds the Coulomb repulsion force between protons, and its range is a few fm (fm = 10^{-15} m) which is much shorter than that of the Coulomb force and comparable with the average distance between nucleons in a nucleus. As a result, the density of the nucleus and the binding energy per nucleon are well-saturated. Despite the strong correlation between nucleons due to the nuclear forces, it is known that the structure of the nucleus is well described by a single-particle picture of the nucleon in the mean-field. The "shell" structure (atom-like structure) of nucleons is the most typical example of the single-particle picture and is especially dominant in the ground state (Fig. 1).

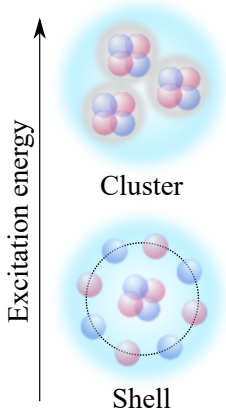

Fig. 1 Schematic figure of shell and cluster structures for ^{12}C as an example. The red and blue circles are proton and neutron, respectively.

On the other hand, the structure of the excited states, especially in the light-mass region, can be drastically changed to "cluster" structure (molecule-like structure) with a small amount of excitation energy (see also Fig. 1). In the cluster structure, a group of nucleons is strongly bound to form the sub-unit called "cluster". This cluster structure state is a universal phenomenon in atomic nuclei. The most typical cluster is ^{4}He nucleus called α particle which consists of two protons and two neutrons

due to its spin-isospin saturated and double-closed shell structure. The presence of α particles in the nuclear state has been discussed since the 1930s [2,3]. Table 1 lists the binding energy per nucleon (B.E./A) and the first excited state energy E_x^{1st} for light nuclei. The B.E./A of α particle is much larger than that of the other light nuclei and close to the saturation energy 8 MeV. Furthermore, the E_x^{1st} of the α particle is approximately 20 MeV which is remarkably larger than the other light nuclei, which means the stiffness of α particle as a sub-unit.

Tab. 1 Binding energy per nucleon (B.E./A) and first excited state energy E_x^{1st} in the unit of MeV.

	B.E./A	E_x^{1st}
^{3}He	2.57	-
α	7.07	20.21
^{6}He	4.88	1.80
^{8}He	3.92	2.92
^{2}H	1.11	-
^{3}H	2.83	-

In order to explain in which excitation energy region the cluster structure states of α particles can appear, a threshold rule (or hypothesis) was proposed half a century ago [4]. The rule insists that when a cluster structure state emerges, it appears the corresponding decomposition threshold energy. This rule also indicates that when the excitation energy is lower than the cluster decomposition threshold, the cluster loses its identity and the shell structure becomes dominant. Figure 2 is a so-called Ikeda diagram that shows how cluster structures emerge according to the threshold rule for the self-conjugate nuclei (mass number $A = 4n$ where $Z = N = 2n$ and $n \in \mathbb{N}$).

1.2 Molecular orbit model

The cluster structure of the nucleus with excess neutrons becomes more complicated. α cluster structures also emerge in neutron-rich nuclei, and the role of excess neutrons in these nuclei is an intriguing study. Namely, the excess neutrons in neutron-rich nuclei stabilize unstable cluster structures such as the linear-chain configuration in which two or more clusters are linearly aligned. The extended Ikeda diagram was proposed [5] to explain the role of excess neutrons in neutron-rich nuclei as shown in Fig. 3. The number of possible cluster structures is much larger than that in the self-conjugate nuclei. Be isotopes are a well-known example for explaining the role of the excess neutrons which surround the 2α particle cores and stabilize the nuclei [5–9]. ^{8}Be has a well-developed cluster structure consisting of 2α particles and is an unstable nucleus that decays into 2α particles. On the other hand, both ^{9}Be and ^{10}Be having

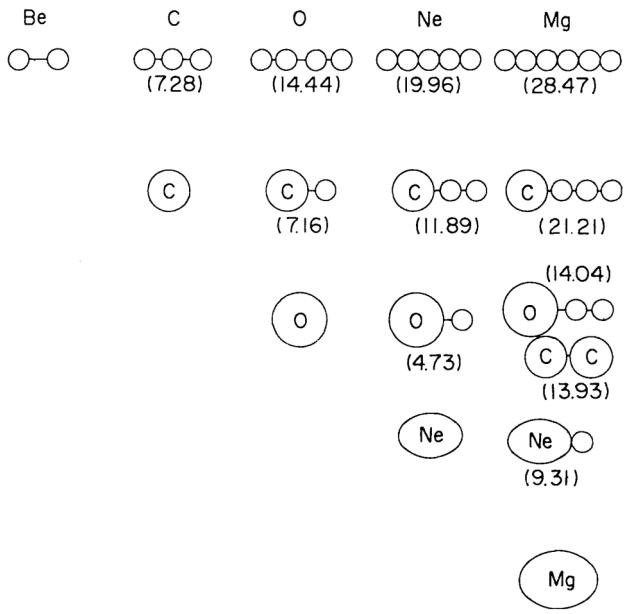

Fig. 2 Ikeda diagram proposed in Ref. [4]. The values mean the excitation energies of α cluster-decay thresholds in the unit of MeV. The open circle shows the α particle. The nucleus is dissolved into α particle units by providing energy.

one and two additional neutrons are stable nuclei and are famous examples of the α clustering. The distance between the 2α particles in ^{9}Be and ^{10}Be is shorter than that of ^{8}Be. Thus, the excess neutrons in ^{9}Be and ^{10}Be play a *glue*-like role. Furthermore, ^{11}Be and ^{12}Be having more additional neutrons have more developed cluster structures than ^{10}Be [10, 11]. These discussions on the enhancement of the cluster structures in neutron-rich Be isotopes are consistent with the experimental charge radii [12–14]. Therefore, the excess neutrons play an important role in enhancing as well as bonding the cluster structures.

This emergence mechanism of the cluster structures in Be isotopes can be explained by the molecular orbits of the excess neutrons that are formed around the 2α cores. Figure 4 shows the p-orbits constructed around the α particle (panel (a)) and corresponding nucleon orbits in the mean-field in which two protons and two neutrons forming the α particle occupy the s-orbit and a single excess neutron occupies the p-orbit (panel(b)). In Be isotopes consisting of 2α cores and the excess neutrons, the systems are expected to be described by a linear combination of the p-orbits constructed around the α core (Fig. 5(a)) because the p-orbit is the lowest allowed orbit around the α particle. As a result, two types of orbits of the excess neutrons are constructed around the 2α cores and are called σ-orbit and π-orbit following the manner in the covalent electron orbits in molecules. The π-orbit with negative parity is the lowest nodal orbit with a single node in the transverse direction for the α-α direc-

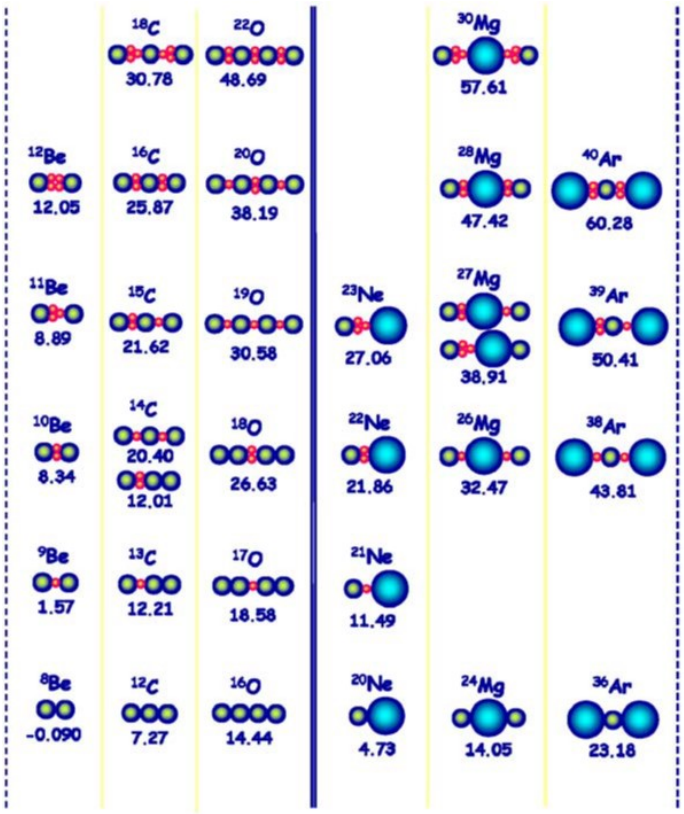

Fig. 3 Extended Ikeda diagram (as in Fig. 2) for neutron-rich nuclei as well as self-conjugate nuclei. Some molecular structures consisting of α particles and ^{16}O nuclei clusters with valence neutrons are shown. The schematic shapes are given with the threshold energies for the decomposition into the continuum state. This figure is taken from Ref. [5].

tion and shortens the 2α core distance while the positive parity σ-orbit is the higher nodal orbit in the longitudinal direction and enhances the 2α cluster structure. Using this molecular orbit picture, the development of the cluster structure in Be isotopes can be explained more clearly. In the ground states of ^{9}Be and ^{10}Be, the 2α cluster structure is hindered due to the one and two excess neutrons occupying the π-orbit, respectively, compared with that of ^{8}Be ground state. As a result, the ground states of ^{9}Be and ^{10}Be become bound states, which indicates that one or more excess neutrons play a role in stabilizing the 2α system. On the other hand, in the ground states of ^{11}Be and ^{12}Be, the 2α core distance is elongated because of the additional excess neutrons occupying the σ-orbit showing the well-developed cluster structures. At the same time, the cluster structures in not ground but excited states of Be isotopes are also discussed [15] in which, for example, various "ionic" configurations are predicted in ^{12}Be such as α + ^{8}He, ^{6}He + ^{6}He, and ^{5}He + ^{7}He configurations.

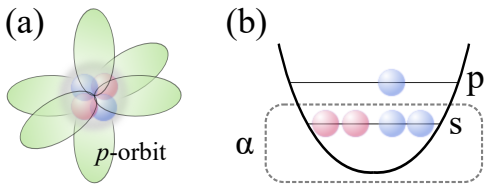

Fig. 4 (a) p-orbits constructed around the α particle. (b) Corresponding nucleon orbits in the mean-field. Namely, two protons and two neutrons forming the α particle occupy the s-orbit and the third excess neutron occupies the p-orbit.

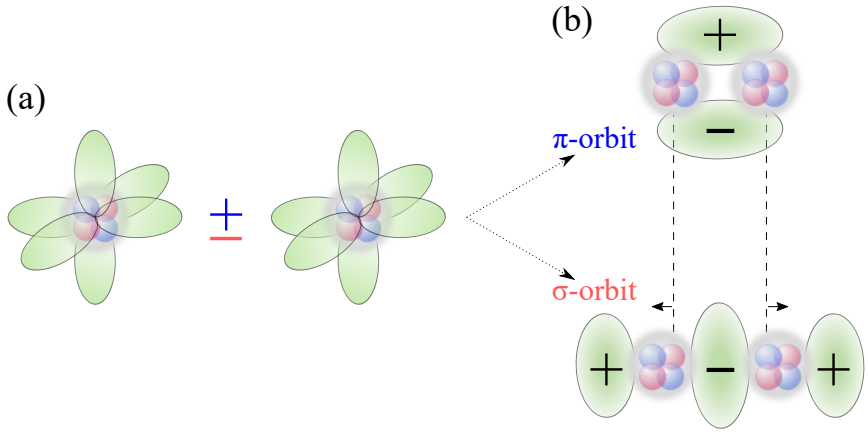

Fig. 5 (a) Linear combination of two α cores with the p-orbits occupied by the excess neutron. (b) σ-orbit and π-orbit constructed around the 2α cores.

1.3 Studies on cluster formation in isotope chain

1.3.1 Measurement of α cluster structure

α particle plays a significant role in such as the α decay in heavy nuclei and the astrophysical nuclear reaction in light nuclei. Thus, it is an important issue how to experimentally verify the α cluster structure in the nucleus. The proton-induced α knockout reaction (p, $p\alpha$) has been utilized for years to investigate the α cluster formation in the ground state of nuclei [16, 17] since it can be considered that the larger the cross section of the (p, $p\alpha$) experiment, the more α particles are present in the nucleus. However, there is a problem, for example, that α spectroscopic factors (S-factors) deduced from α knockout experiments using the reaction theories and phenomenological α cluster wave functions do not agree with that of the cluster model calculations [17]. Specifically, a large discrepancy of the α S-factor in ^{20}Ne, known as a nucleus having α+^{16}O structure and well described by the AMD framework, was reported between that estimated from the ^{20}Ne(p, $p\alpha$)^{16}O experiment (Fig. 6(a)) and

that calculated from cluster model calculations. This discrepancy was successfully solved several years ago [18]. In Fig. 6(b), it is shown that the triple differential cross-section (TDX) of the ^{20}Ne(p, $p\alpha$)^{16}O reaction is reproduced by the reaction theory and the AMD+RWA framework (see Sec. 2). The authors also evaluated the real part of the transition matrix density using a peak of the TDX (Fig. 6(c)) to show a "radial distribution of the cross-section". R is a sum of the calculated matter radii of α and ^{16}O. This means that the surface region of ^{20}Ne contributes to the (p, $p\alpha$) cross-section because the internal region of the presented line is much suppressed by the absorption effect. Therefore, the proton-induced α knockout reaction is a quantitative probe for the α cluster formation at the nuclear surface. Recently, this (p, $p\alpha$) reaction has been also applied to heavier nuclei such as ^{112,116,120,124}Sn [19] ($Z = 50$) and ^{210,212}Po ($Z = 84$) [20] in the interest of α decay and determining the equation of state (EoS) of the matter. On the other hand, the experiments for assessing the ^{6}He and ^{8}He cluster structures have not yet been established.

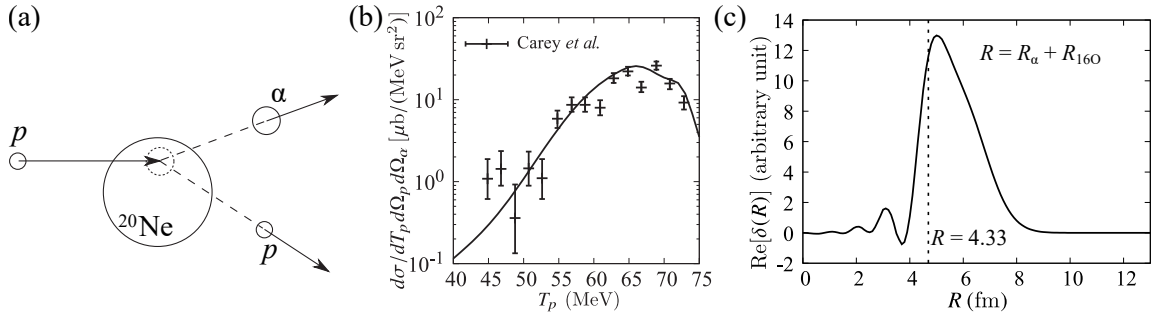

Fig. 6 (a) Schematic figure of the (p, $p\alpha$) reaction for ^{20}Ne target. (b) Energy sharing distribution calculated by DWIA with the AMD+RWA compared with the experiment [17]. Namely, the triple differential cross section for the reaction as a function of the proton emission energy T_p. (c) Real part of the transition matrix density defined by [21] at the recoil-less condition ($T_p = 67$ MeV). All panels are taken from Ref. [18] and modified.

1.3.2 Cluster formation in heavy nuclei

Many unstable nuclei decay by emitting an α particle, which is called α decay and is theoretically explained by a quantum tunneling of the α particle formed within the nucleus. However, the mechanism of how α particles are formed in heavy nuclei has not been elucidated to date. Theoretically, the α density distributions were investigated for ^{112,116,120,124}Sn isotopes (Fig. 7(a)) [22]. These peak positions are slightly outside of $r \sim 6.2$ fm which is a sum of the charge radii of α and corresponding Cd isotopes. Therefore, it was predicted that the formation of α particles develops at the surface of nuclei where the density is dilute approximately 1/10 of the saturation

density (Fig. 7(b)). Motivated by this prediction, the $(p,\ p\alpha)$ reaction experiments for the Sn isotopes have been conducted [19]. Specifically, the ground-state to the ground-state channel ^{A}Sn(g.s.)$(p,\ p\alpha)^{A-4}$Cd(g.s.) was evaluated for $A = 112, 116, 120, 124$. Figure 8(a) shows the missing-mass spectra for the $(p,\ p\alpha)$ reaction for ^{112}Sn target and the Gaussians fit for the peaks of the ^{108}Cd ground-state, which indicates that α particles are formed at the surface of ^{112}Sn(g.s.). The same results were reported for the other Sn isotopes (^{116,120,124}Sn). As a result, the existence of α particles was experimentally confirmed in the ^{112,116,120,124}Sn isotopes. Figure 8(b) shows that the cross sections of the $(p,\ p\alpha)$ reaction decrease as the neutron number, which is correlated with the neutron-skin thickness, increases [22]. Thus, a negative correlation between the neutron-skin thickness and the α cluster formation has been reported as theoretically predicted.

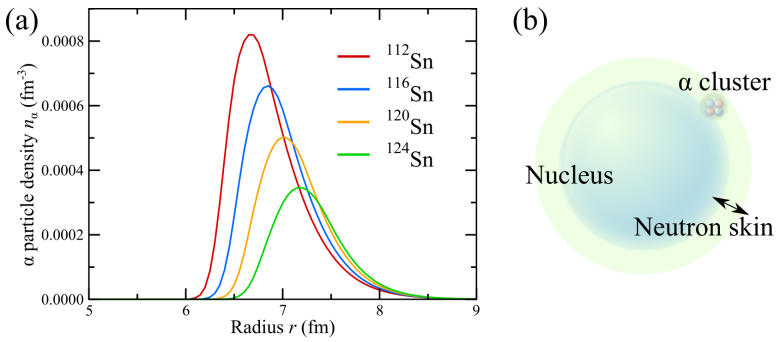

Fig. 7 (a) Radial density distribution of α particles for ^{112,116,120,124}Sn. (b) Schematic figure of α cluster at the nuclear surface of the neutron-rich nucleus. The neutron-skin thickness is defined by the difference between the neutron and proton radii. Panel (a) is taken from Ref. [22] and modified.

1.3.3 Cluster formation in light nuclei

A similar negative correlation was also theoretically predicted in neutron-rich C isotopes by directly analyzing the S-factors of the α cluster [23]. In contrast to the trend observed in Sn isotopes and calculated in C isotopes, the α cluster formation in light nuclei, such as Be and B isotopes, is predicted to enhance as the neutron drip-line approaches [10, 11, 24–27]. In the previous studies, the development of the α cluster formation is discussed based on the distance between the two cores in the proton density distributions $\rho_{\rm p}$ and the proton distribution radii. The position of the core in the distribution $\rho_{\rm p}$ can be regarded as the position of the α particle since the distribution $\rho_{\rm p}$ is almost evenly distributed over the two cores (Fig. 9(a)). Thus, α cluster formation in Be isotopes is expected to be enhanced as the neutron number increases beginning at ^{10}Be. This trend is not inconsistent with the observed charge

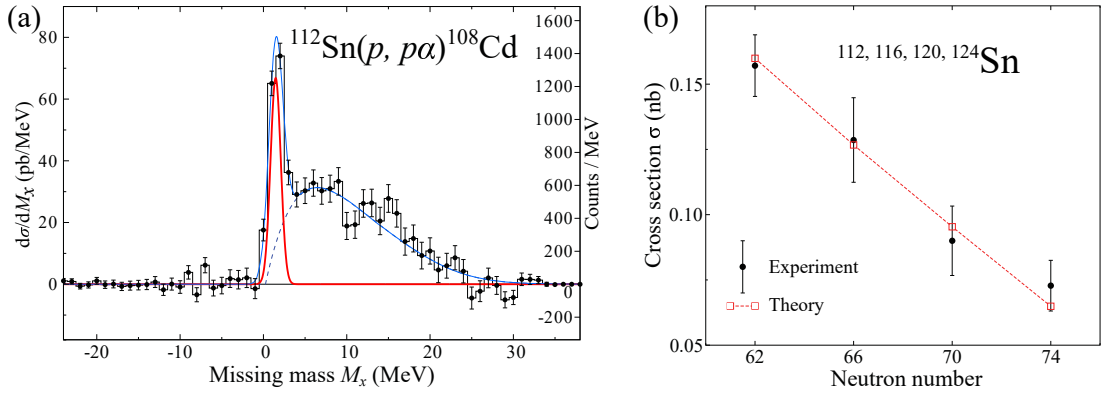

Fig. 8 (a) Missing-mass ($M_x \equiv m_\alpha + m_{\rm Cd} - m_{\rm Sn}$) spectra for the α-knockout reaction for ^{112}Sn target. The blue line represents the result of the fit with the Gaussians for the ground-state peaks (red line) and the simulated shapes of the continuum (dashed line). (b) Cross sections of the (p, $p\alpha$) reaction for ^{112,116,120,124}Sn as a function of the neutron number compared with the theoretical values [22]. Both panels are taken from Ref. [19] and modified.

radii [12–14] (Fig. 9(b)). Similar development of the α cluster formation has been discussed for B isotopes where the two cores also appear in the proton density distributions [10,11]. Specifically, it was reported that α cluster formation in B isotopes is expected to enhance as the neutron drip-line approaches from ^{11}B. However, the proton density distributions and the radii do not directly evaluate the α cluster formation because the α particle is composed of not only two protons but also two neutrons. Furthermore, the neutron density distributions $\rho_{\rm n}$ are well-varied compared with that of protons (Fig. 9(a)).

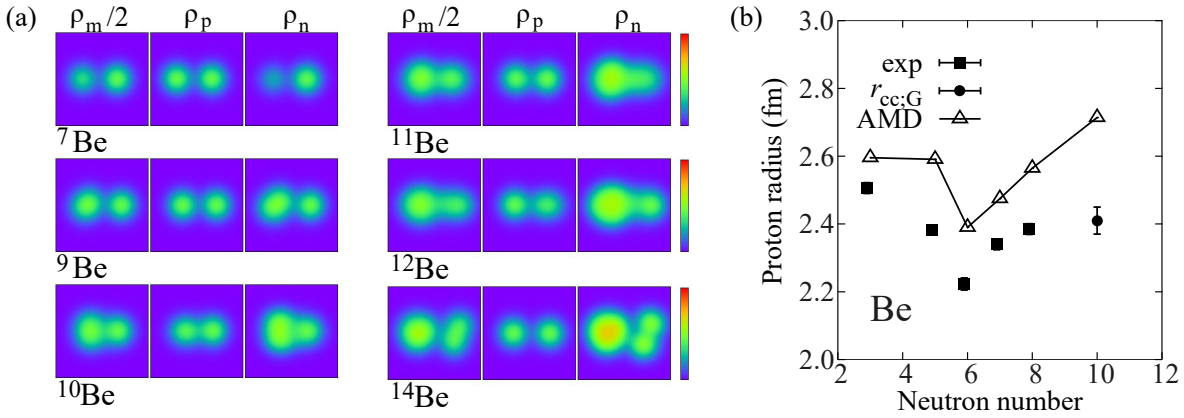

Fig. 9 (a) Proton, neutron, and matter density distributions ρ of Be isotopes calculated by the AMD+VAP framework. (b) Those proton distribution radii compared with the experimental values. Both panels are taken from Ref. [10] and modified.

1.4 Purpose of this study

The experiments show a negative correlation between the α cluster formation and neutron number in Sn isotopes using the $(p,\ p\alpha)$ reaction. In contrast, the opposite trend is theoretically predicted in Be and B isotopes based on the proton density distributions ρ_{p} and the radii. Although the observed charge radii of the Be and B isotopes appear to correlate with the distance between the two cores in the distributions ρ_{p} and also the radii, these calculated values themselves are not physical quantity that allows direct probing of the α cluster structure. Therefore, studying physical quantities that can directly probe the cluster structure is highly desirable. In this study, focusing on the opposite trends of the α cluster formation, I directly investigate the α cluster formation in Be and B isotopes toward the neutron drip-line to elucidate the effects of the excess neutrons on the α cluster formation. For this purpose, the α cluster formation is evaluated by the α S-factors, which can be experimentally measured via $(p, p\alpha)$ reactions, in Be and B isotopes using the antisymmetrized molecular dynamics (AMD) framework.

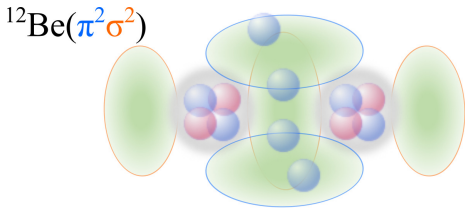

Fig. 10 Schematic figure of ^{12}Be where the σ- and π-orbits are occupied by the two excess neutrons (blue circles), respectively.

In Be isotopes, the molecular orbits occupied by the excess neutrons play a "covalent bond"-like role. Figure 10 schematically shows ^{12}Be as an example where the σ- and π-orbits are occupied by the two excess neutrons, respectively. This allows considering the conjecture that the residual nucleus ^{8}He may be excited when the α particle is kicked out. However, a channel related to the excited residual nucleus can not be measured by the $(p, p\alpha)$ reaction since the reaction is limited to the channel between the ground states only. Additionally, ^{6}He+^{6}He configuration is expected to emerge owing to the excess neutrons surrounding the two α cores. In a similar manner, ^{6}He cluster is also expected to play an essential role in the enhancement of the Be isotopes. According to previous studies, many B isotopes must have two α cores and the excess neutrons surround the two cores, which indicates that ^{6}He and ^{8}He clusters have an influence on the enhancement of the B isotopes.

Another point is that the closer the isotope is to the neutron drip-line, the less bound the residual nucleus corresponding to the α particle becomes although there

are exceptions. For example, ^{10}He is a residual nucleus corresponding to the α particle in ^{14}Be and it is known as an unbound nucleus in free space, which indicates that the clustered structure consisting of the bound nuclei is likely to emerge, i.e., ^{6}He+^{8}He configuration. Likewise, ^{13}Li is a residual nucleus corresponding to the α particle in ^{17}B and it is known as an unbound nucleus in free space.

With these conjectures, ^{6}He and ^{8}He clusters are also taken into account as well as the α clusters to elucidate the effects of the excess neutrons on the α cluster formation. Since ^{6}He and ^{8}He clusters are composed of a single α core and the excess neutrons, those S-factors in Be and B isotopes enable us to discuss how much α cluster structure is enhanced having the excess neutrons which surround the α cores. This analysis of ^{6}He and ^{8}He cluster formations is the novelty of this study.

2 Theoretical Framework

2.1 Effective Hamiltonian

The microscopic Hamiltonian for A-body system is expressed as,

$$\hat{H} = \sum_{i}^{A} \hat{t}(\boldsymbol{r}_i) - \hat{t}_{\text{c.m.}} + \sum_{i<j}^{A} \hat{v}_{\text{NN}}(\boldsymbol{r}_{ij}) + \sum_{i<j\in\text{proton}}^{A} \hat{v}_{\text{C}}(\boldsymbol{r}_{ij}), \tag{2.1}$$

where $\hat{t}_i$ and $\hat{t}_{\text{c.m.}}$ denote the nucleon and center-of-mass kinetic energies, respectively. $\hat{v}_{\text{C}}$ is a Coulomb interaction approximated by a sum of seven Gaussians. The Gogny D1S parameter set [28] is employed to represent the effective nucleon-nucleon interaction $\hat{v}_{\text{NN}}$,

$$\begin{aligned}\hat{v}_{\text{NN}}(\boldsymbol{r}_{ij}) = &\sum_{k=1,2} (W_k + B_k\hat{P}_\sigma - H_k\hat{P}_\tau - M_k\hat{P}_\sigma\hat{P}_\tau) \exp\left[-\left(\frac{\boldsymbol{r}_i - \boldsymbol{r}_j}{\mu_k}\right)^2\right] \\ &+ iW_{LS}\overleftarrow{\nabla}\delta(\boldsymbol{r}_i - \boldsymbol{r}_j) \times \overrightarrow{\nabla} \cdot (\boldsymbol{\sigma}_i + \boldsymbol{\sigma}_j) \\ &+ v_{DD}(1 + \hat{P}_\sigma)\delta(\boldsymbol{r}_i - \boldsymbol{r}_j)\left[\rho\left(\frac{\boldsymbol{r}_i + \boldsymbol{r}_j}{2}\right)\right]^{1/3},\end{aligned} \tag{2.2}$$

where the first term is a central force with finite range interaction expressed as a sum of the attractive and repulsive nuclear force. The $\hat{P}_\sigma$ and $\hat{P}_\tau$ represent the spin and isospin exchange operator, respectively. Thus, the W, B, H, and M are the coefficients of direct, spin exchange, isospin exchange, and spin-isospin exchange terms, respectively. The second term is a zero-range two-body spin-orbit interaction where $\overleftarrow{\nabla}$ and $\overrightarrow{\nabla}$ act on the bra and ket side, respectively. The final one is a functional of nuclear density ρ.

2.2 AMD wave function

The model wave function of the A-body system is represented by a Slater determinant of single-particle wave packets,

$$\Phi_{\text{AMD}} = \mathcal{A}\{\varphi_1\ \varphi_2\ \cdots\ \varphi_A\} = \frac{1}{\sqrt{A!}} \begin{vmatrix} \varphi_1(\boldsymbol{r}_1) & \cdots & \varphi_A(\boldsymbol{r}_1) \\ \vdots & \ddots & \vdots \\ \varphi_1(\boldsymbol{r}_A) & \cdots & \varphi_A(\boldsymbol{r}_A) \end{vmatrix}, \tag{2.3}$$

where φ_i is the i-th single particle wave packet which is composed of the spatial ϕ_i, spin χ_i, and isospin η_i parts,

$$\varphi_i(\boldsymbol{r}) = \phi_i(\boldsymbol{r})\chi_i\eta_i, \tag{2.4}$$

$$\phi_i(\boldsymbol{r};\boldsymbol{Z}) = \phi_i(\boldsymbol{r}) = \prod_{\sigma=x,y,z}\left(\frac{2\nu_\sigma}{\pi}\right)^{1/4}\exp\left\{-\nu_\sigma(r_\sigma - Z_{i\sigma})\right\}^2, \tag{2.5}$$

$$\chi_i = a_i\chi_\uparrow + b_i\chi_\downarrow, \quad |a_i|^2 + |b_i|^2 = 1, \tag{2.6}$$

$$\eta_i = \text{proton or neutron}. \tag{2.7}$$

The spatial part ϕ_i is expressed by deformed Gaussian [29]. The Gaussian widths ν_σ, centroids $Z_{i\sigma}$, and spin directions a_i, b_i are the variational parameters. The AMD wave function Eq. (2.3) can be decomposed into the intrinsic wave function $\Phi_{\rm int}$ and the center-of-mass wave function $\Phi_{\rm cm}$:

$$\Phi_{\rm AMD} = \Phi_{\rm int}\Phi_{\rm cm}, \tag{2.8}$$

$$\Phi_{\rm int} = \frac{1}{\sqrt{A!}}\begin{vmatrix} \varphi_1(\boldsymbol{r}'_1) & \cdots & \varphi_A(\boldsymbol{r}'_1) \\ \vdots & \ddots & \vdots \\ \varphi_1(\boldsymbol{r}'_A) & \cdots & \varphi_A(\boldsymbol{r}'_A) \end{vmatrix}, \tag{2.9}$$

$$\Phi_{\rm cm} = \prod_{\sigma=x,y,z}\left(\frac{2A\nu_\sigma}{\pi}\right)^{1/4}\exp\left\{-\nu_\sigma r^2_{{\rm cm},\sigma}\right\}. \tag{2.10}$$

where $\Phi_{\rm cm}$ is renormalized. The center-of-mass coordinate $\boldsymbol{r}_{\rm cm}$ and relative coordinate $\boldsymbol{r}'_i = \boldsymbol{r}_i - \boldsymbol{r}_{\rm cm}$ satisfy the relation $\boldsymbol{r}_{\rm cm} = \frac{1}{A}\sum_{i=1}^{A}\boldsymbol{r}_i$. The details of this decomposition and the expectation values of the operators sandwiched by $\Phi_{\rm int}$ are explained in Appendices A.1 and A.2, respectively.

The parity-projected wave function is employed as the variational wave function,

$$\Phi^\pi = \hat{P}^\pi\Phi_{\rm int} = \frac{1+\pi\hat{P}_x}{2}\Phi_{\rm int}, \tag{2.11}$$

where $\hat{P}^\pi$ denotes the parity projection operator. The variational parameters of Eq. (2.4) are independently determined for each parity by the variational calculation with the shape constraint explained in Sec. 2.3.

2.3 Variational calculation with a shape constraint

A variational calculation is performed under constraint on the matter quadrupole deformation parameter β.

The variational parameters X_i (ν_σ, $Z_{i\sigma}$, a_i, and b_i) are determined by the frictional cooling method [30] which minimizes the energy $\tilde{E}(X_i, X_i^*)$. The variables X_i follow

the equation of motion,

$$-i\hbar\frac{\mathrm{d}X_i}{\mathrm{d}t} = \mu\frac{\partial\tilde{E}}{\partial X_i^*} \tag{2.12}$$

where μ is the positive real number. Suppose that t is the pure imaginary number $t = i\tau$, the function $\tilde{E}(X_i, X_i^*)$ is minimized by developing the imaginary time τ,

$$\frac{\mathrm{d}}{\mathrm{d}\tau}\tilde{E}(X_i, X_i^*) = \sum_i \left(\frac{\partial\tilde{E}}{\partial X_i}\frac{\mathrm{d}X_i}{\mathrm{d}\tau} + \frac{\partial\tilde{E}}{\partial X_i^*}\frac{\mathrm{d}X_i^*}{\mathrm{d}\tau}\right) = -\frac{2\mu}{\hbar}\sum_i \left|\frac{\partial\tilde{E}}{\partial X_i}\right|^2 \leq 0. \tag{2.13}$$

In the AMD framework, the energy $\tilde{E}$ is defined as,

$$\tilde{E}(\beta) = \frac{\langle\Phi^\pi(\beta)|\hat{H}|\Phi^\pi(\beta)\rangle}{\langle\Phi^\pi(\beta)|\Phi^\pi(\beta)\rangle} + v_\beta(\langle\beta\rangle - \beta)^2, \tag{2.14}$$

where the parabolic potential is added to the total energy to impose the β constraint and the constraint potential strength v_β is selected sufficiently large positive value. The β and $\langle\beta\rangle$ are the quadrupole deformation parameter as an input constraint value and the expectation value of β calculated by Eq. (2.15) [31] explained below, respectively. The Eq. (2.14) is ideally minimized when the $\langle\beta\rangle$ is equal to the input β. Then one obtains the optimized wave function $\Phi^\pi(\beta)$ which has the minimum energy for each given value of β. In this calculation, the input constraint values β are $\beta = 0.00,\ 0.05, \cdots,\ 0.90$.

The quadrupole deformation parameters β and γ are defined as,

$$\langle\hat{\sigma}^2\rangle = R_0^2\left[1 + \sqrt{\frac{5}{\pi}}\langle\beta\rangle\cos\left\{\langle\gamma\rangle + (-)^{\delta_{y\sigma}}(1-\delta_{z\sigma})\frac{2\pi}{3}\right\}\right], \tag{2.15}$$

$$R_0^2 = \frac{1}{3}\sum_{\sigma=x,y,z}\langle\hat{\sigma}^2\rangle, \tag{2.16}$$

where $\langle\hat{\sigma}^2\rangle$ is the expectation value of the squared radius in the σ-direction $\langle\Phi^\pi|\hat{\sigma}^2|\Phi^\pi\rangle$ and R_0 is the radius of the spherical nucleus. Here, the relation $R_x \leq R_y \leq R_z$ is satisfied. The second term of Eq. (2.15) expresses the deviation from the sphere of radius R_0. The parameters β and γ represent the deformation of the entire nucleus and the relationship among the lengths of the three principal axes of the ellipsoid, respectively. Figure 11 shows a part of β-γ plane but this part is consistent with the other parts of the plane with different principal axes. The typical shapes are conventionally named as follows.

(a) Spherical: $\beta = 0$, $\gamma = 0$ (deg.); $\langle\hat{x}^2\rangle = \langle\hat{y}^2\rangle = \langle\hat{z}^2\rangle$
(b) Prolate: $\beta \neq 0$, $\gamma = 0$ (deg.); $\langle\hat{x}^2\rangle = \langle\hat{y}^2\rangle < \langle\hat{z}^2\rangle$

(c) Oblate: $\beta \neq 0$, $\gamma = 60$ (deg.); $\langle \hat{x}^2 \rangle = \langle \hat{y}^2 \rangle > \langle \hat{z}^2 \rangle$

The prolate and oblate shapes show an axisymmetric deformation with a rotationally symmetric axis. In this calculation, z-axis is employed as a rotationally symmetric axis.

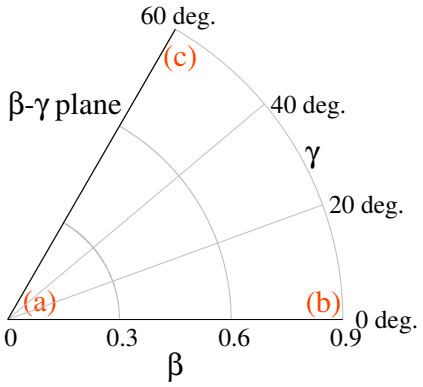

Fig. 11 β-γ plane. (a), (b), and (c) show the region of the spherical, prolate, and oblate shapes shown in Fig. 12, respectively.

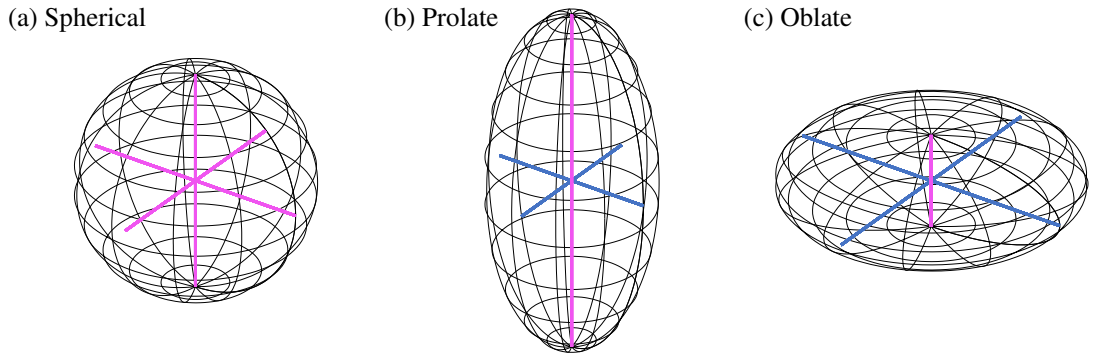

Fig. 12 Schematic figures showing the quadrupole deformation of a nucleus. (a), (b), and (c) show the spherical, prolate, and oblate shapes corresponding to Fig. 11, respectively.

2.4 Angular momentum projection

The optimized wave functions $\Phi^{\pi}(\beta)$ obtained by the energy variational calculation have deformed shapes and therefore break the rotational symmetry. Thus, $\Phi^{\pi}(\beta)$ is projected onto the eigenstate of the total angular momentum J to restore the

rotational symmetry breaking,

$$\Phi^{J\pi}_{MK}(\beta) = \frac{2J+1}{8\pi^2}\int \mathrm{d}\Omega\, D^{J\,*}_{MK}(\Omega)\hat{R}(\Omega)\Phi^{\pi}(\beta), \tag{2.17}$$

$$D^{J}_{MK}(\Omega) = \langle JM|\hat{R}(\Omega)|JK\rangle, \tag{2.18}$$

$$\hat{R}(\Omega) = e^{-i\alpha\hat{J}_z}e^{-i\beta\hat{J}_y}e^{-i\gamma\hat{J}_z}, \tag{2.19}$$

where $D^{J}_{MK}(\Omega)$ and $\hat{R}(\Omega)$ denote the Wigner's D-function and the rotation operator. This integral calculation over Euler angles Ω is numerically evaluated. Then, one obtains the spin-parity-projected wave functions $\Phi^{J\pi}_{MK}(\beta)$ which have a different value of the deformation parameter β.

2.5 Generator coordinate method

The generator coordinate method (GCM) is adopted to obtain the wave functions and energies employing the deformation parameter β as the generator coordinate. The GCM wave function is expressed as the superposition of the spin-parity-projected wave functions $\Phi^{J\pi}_{MK}(\beta)$,

$$\Psi^{J\pi}_{M,\alpha} = \sum_{iK} g_{iK,\alpha}\Phi^{J\pi}_{MK}(\beta_i). \tag{2.20}$$

This Eq. (2.20) is the wave function of the generator coordinate method (GCM) [32], where the deformation parameter β is employed as the generator coordinate. This GCM wave function can approximately well describe the bound state as well as the unbound state with a bound state approximation. The coefficients $g_{jK',\alpha}$ and the eigenenergy E_α are determined by solving the Hill-Wheeler equation [32],

$$\sum_{jK'}(H_{iKjK'} - E_\alpha N_{iKjK'})g_{jK',\alpha} = 0, \tag{2.21}$$

$$H_{iKjK'} = \langle\Phi^{J\pi}_{MK}(\beta_i)|\hat{H}|\Phi^{J\pi}_{MK'}(\beta_j)\rangle, \tag{2.22}$$

$$N_{iKjK'} = \langle\Phi^{J\pi}_{MK}(\beta_i)|\Phi^{J\pi}_{MK'}(\beta_j)\rangle. \tag{2.23}$$

The GCM wave functions can be used to derive the properties of Be and B isotopes, such as the distribution radii and degree of clustering.

The overlap between the spin-parity-projected wave function $\Phi^{J\pi}_{MK}(\beta)$ and GCM wave function $\Psi^{J\pi}_{M,\alpha}$ is defined to evaluate how well the GCM wave function can be understood by a single wave function $\Phi^{J\pi}_{MK}(\beta)$,

$$\mathcal{O}_{iK,\alpha} = |\langle\Phi^{J\pi}_{MK}(\beta_i)|\tilde{\Psi}^{J\pi}_{M,\alpha}\rangle|^2, \tag{2.24}$$

$$|\tilde{\Psi}^{J\pi}_{M,\alpha}\rangle = \sum_{iK} g_{iK,\alpha}|\Phi^{J\pi}_{MK}(\beta_i)\rangle/\sqrt{\langle\Phi^{J\pi}_{MK}(\beta_i)\rangle|\Phi^{J\pi}_{MK}(\beta_i)\rangle}. \tag{2.25}$$

2.6 Reduced width amplitude and its radius

To evaluate the degree of clustering in Be and B isotopes, I calculated the reduced width amplitude (RWA), which is generally defined as the overlapping between the A-body GCM wave function $\Phi^{J\pi}_{MA}$ and the reference state composed of the cluster $\Phi^{j_1\pi_1}_{m_1C_1}$ with a mass C_1 and the daughter nucleus $\Phi^{j_2\pi_2}_{m_2C_2}$ with a mass $C_2 = A - C_1$:

$$\mathcal{Y}^{J\pi}_{j_1\pi_1 j_2\pi_2 j_{12}\ell}(a) = n(C_1, C_2) \left\langle \tfrac{\delta(r-a)}{ra} \Big[Y_{\ell m_\ell}(\hat{\boldsymbol{r}}) \big[\Phi^{j_1\pi_1}_{m_1C_1} \Phi^{j_2\pi_2}_{m_2C_2} \big]_{j_{12}m_{12}} \Big]_{JM} \Big| \Phi^{J\pi}_{MA} \right\rangle, \tag{2.26}$$

where $n(C_1, C_2)$ is the normalization constant: $n(C_1, C_2) \equiv \sqrt{\frac{1}{1+\delta_{C_1C_2}} \frac{A!}{C_1!C_2!}}$. It is assumed that the wave functions $\Phi^{J\pi}_{MA}$, $\Phi^{j_1\pi_1}_{m_1C_1}$, $\Phi^{j_2\pi_2}_{m_2C_2}$ are normalized. The spins j_1 and j_2 are coupled to j_{12} with the Clebsch–Gordan coefficient $C^{j_{12}m_{12}}_{j_1m_1j_2m_2}$,

$$\Big[|j_1m_1\rangle |j_2m_2\rangle \Big]_{j_{12}m_{12}} = \sum_{m_1m_2} C^{j_{12}m_{12}}_{j_1m_1j_2m_2}, \tag{2.27}$$

and j_{12} is coupled to the orbital angular momentum ℓ of the inter-cluster motion to yield the total spin-parity J^π. Therefore, the parity conservation $\pi = \pi_1\pi_2(-)^\ell$ is satisfied for π_1, π_2, and ℓ. Thus, the RWA is the probability amplitude of a cluster at a distance $r = a$ from the daughter nucleus. Using the relation combined with the Laplace expansion (see also Appendix A.5),

$$\begin{aligned} \Phi_{\rm int} = \sqrt{\tfrac{C_1!C_2!}{A!}} \sum_{1\le i_1\le\cdots<i_{C_1}\le A} & P(i_1, \cdots, i_{C_1}) \\ & \times \chi(\boldsymbol{r}; i_1, \cdots, i_A) \Phi^{C_1}_{\rm int}(i_1, \cdots, i_{C1}) \Phi^{C_2}_{\rm int}(i_{C_1+1}, \cdots, i_A) \end{aligned} \tag{2.28}$$

the RWA Eq. (2.26) is reduced to,

$$\begin{aligned} \mathcal{Y}^{J\pi}_{j_1\pi_1 j_2\pi_2 j_{12}\ell}(a) = \tfrac{1}{\sqrt{1+\delta_{C_1C_2}}} & \sum_{1\le i_1\le\cdots<i_{C_1}\le A} P(i_1, \cdots, i_{C_1}) \\ \times \Big[\chi_{\ell m_\ell}(a; i_1, \cdots, i_A) & \big[N^{j_1\pi_1}_{m_1}(i_1, \cdots, i_{C1}) N^{j_2\pi_2}_{m_2}(i_{C_1+1}, \cdots, i_A) \big]_{j_{12}} \Big]_{JK}, \end{aligned} \tag{2.29}$$

which corresponds to Eq. (28) in Ref. [33]. Each overlap is defined as,

$$\chi_{\ell m_\ell}(a; i_1, \cdots, i_A) = \left\langle \tfrac{\delta(r-a)}{ra} Y_{\ell m_\ell}(\hat{\boldsymbol{r}}) \Big| \chi(\boldsymbol{r}; i_1, \cdots, i_A) \right\rangle, \tag{2.30}$$

$$N^{j_1\pi_1}_{m_1}(i_1, \cdots, i_{C1}) = \langle \Phi^{j_1\pi_1}_{m_1C_1} | \Phi^{C_1}_{\rm int}(i_1, \cdots, i_{C1}) \rangle, \tag{2.31}$$

$$N^{j_2\pi_2}_{m_2}(i_{C_1+1}, \cdots, i_A) = \langle \Phi^{j_2\pi_2}_{m_2C_2} | \Phi^{C_2}_{\rm int}(i_{C_1+1}, \cdots, i_A) \rangle, \tag{2.32}$$

where $\chi(\boldsymbol{r}; i_1, \cdots, i_A)$ is the relative wave function between the two subsystems; $\Phi^{C_1}_{\rm int}(i_1, \cdots, i_{C1})$ and $\Phi^{C_2}_{\rm int}(i_{C_1+1}, \cdots, i_A)$ are the intrinsic wave function of C_1 and

C_2 clusters, respectively. The degree of clustering may be evaluated by the spectroscopic factor (S-factor), which is defined as the squared integral of the RWA,

$$S(C_1) = \int_0^\infty \mathrm{d}a \left| a\mathcal{Y}^{J\pi}_{j_1\pi_1 j_2\pi_2 j_{12}\ell}(a) \right|^2. \tag{2.33}$$

Notably, $S(C_1)$ is not normalized to unity because of the antisymmetrized effects between the cluster and the daughter nucleus.

In the present study, the spin-parity of cluster C_1 and the orbital angular momentum are $j_1^{\pi_1} = 0^+$ and $\ell = 0$, respectively, which results in the relation: $j_2^{\pi_2} = J^\pi$. Specifically, the spin-parity J^π is 0^+ and $3/2^-$ for the Be and B isotopes, respectively. The RWA Eq. (2.26) and S-factor Eq. (2.33) can be written in a simple formula,

$$\mathcal{Y}_{C_1}(a) = n(C_1, A-C_1) \left\langle \tfrac{\delta(r-a)}{ra} Y_{\ell=0}(\hat{\boldsymbol{r}}) \left[\Phi^{0+}_{C_1} \Phi^{J\pi}_{A-C_1} \right]_J \middle| \Phi^{J\pi}_A \right\rangle, \tag{2.34}$$

$$S(C_1) = \int_0^\infty \mathrm{d}a \left| a\mathcal{Y}_{C_1}(a) \right|^2. \tag{2.35}$$

Only for t+^{8}Be channel in ^{11}B, the RWA Eq. (2.26) is written as,

$$\mathcal{Y}_{C_1=t}(a) = \sqrt{\binom{11}{3}} \left\langle \tfrac{\delta(r-a)}{ra} Y_{\ell=1}(\hat{\boldsymbol{r}}) \left[\Phi^{1/2+}_t \Phi^{0+}_{^8\mathrm{Be}} \right]_{1/2} \middle| \Phi^{3/2-}_{^{11}\mathrm{B}} \right\rangle. \tag{2.36}$$

where isospins of $t(j_1^{\pi_1} = \frac{1}{2}^+)$ were composed of a single proton with up (or down) spin and two neutrons with opposite spins.

The root mean square (RMS) radius of the RWA between the cluster C_1 and the daughter nucleus is defined as,

$$a_{\mathrm{rms}}(C_1) \equiv \left[\int_0^\infty \mathrm{d}a\ a^2 \left| a\mathcal{Y}_{C_1}(a) \right|^2 \Big/ \int_0^\infty \mathrm{d}a \left| a\mathcal{Y}_{C_1}(a) \right|^2 \right]^{1/2}, \tag{2.37}$$

where an expectation value of the squared inter-cluster distance a is normalized by the S-factor, $S(C_1)$.

3 Results and Discussions

3.1 α, ^{6}He, and ^{8}He clusters

In the present study, cluster formations of ^{6}He and ^{8}He clusters in Be and B isotopes are analyzed as well as that of α clusters. In general, the size of a cluster at the nuclear surface might be different from that in free space. However, it was confirmed that the size change of the α cluster is small enough at the surface of several light nuclei and does not affect the magnitude of $S(\alpha)$ [33]. Thus, I have assumed that the α cluster size at the nuclear surface is the same as that in free space. Additionally, the same assumption is imposed for ^{6}He and ^{8}He clusters.

Here, the binding energies and charge radii are listed in Tab. 2 compared with those experimental values. ^{6}He and ^{8}He clusters are described by the AMD+GCM framework explained in section 2 while α cluster is described by a product of Gaussians whose size parameter is chosen to reproduce the observed value of the α radius. The obtained binding energies and charge radii are qualitatively reproduced although the former is slightly overbounded and the latter is slightly overestimated.

Tab. 2 Calculated binding energies (B.E.) and charge radii $\sqrt{\langle r_c^2 \rangle}$ compared with the experimental values in the unit of MeV and fm, respectively.

	B.E.	B.E. (Expt.)	$\sqrt{\langle r_c^2 \rangle}$	$\sqrt{\langle r_c^2 \rangle}$ (Expt.)
α	-29.7	-28.29566240(80)	1.90	1.67824(83) [34]
^{6}He	-32.2	-29.271120(54)	2.16	2.068(11) [35]
^{8}He	-33.0	-31.396168(88)	2.15	1.929(26) [35]

3.2 Cluster formation in Be isotopes

3.2.1 Structure of Be isotopes

Be isotopes are well known to have an enhanced 2α-cluster core surrounded by valence neutrons; such cores have been studied using numerous cluster models [7,9,11,36–38]. In the molecular orbital model, the excess neutrons occupy the molecular orbits and bond with the α particles [6, 39–41]. ^{10}Be is dominated by the π^2 configuration, in which the two excess neutrons occupy the π orbitals corresponding to the spherical p-orbits in the limit of zero distance between the two α clusters. The two additional excess neutrons in ^{12}Be occupy the σ orbitals, which correspond to the spherical sd-shell in the limit of zero distance between the two α clusters; further, the $\pi^2\sigma^2$ configuration is dominant in ^{12}Be. Similarly, the two additional excess neutrons in

^{14}Be occupy the π orbitals, and the $\pi^4\sigma^2$ configuration is dominant. It is considered that the σ-bond structure separates the α particles, while the π-bond structure brings them closer [9,11]. In an ordinary spherical shell model, ^{10}Be and ^{14}Be are dominated by the normal configuration, i.e. the $0\hbar\omega$ configuration. In contrast, ^{12}Be is dominated by the $2\hbar\omega$ configuration, in which two of the valence neutrons occupy the orbits in the *sd*-shell beyond the $N = 8$ shell gap.

The ground-state properties of ^{10}Be, ^{12}Be, and ^{14}Be deduced by our calculations are summarized in Table 3. The point proton or charge distribution radii of the Be isotopes increase toward the neutron drip-line in accordance with the enhancement of clustering. In Fig. 13, both the observed and calculated RMS charge radii increase from ^{10}Be toward the neutron drip-line, although our calculations systematically overestimate the radii. This is because the Gogny interaction used in this study tends to overestimate the radii of the *s*-shell nuclei, in particular that of the α particle, which is an important ingredient of the clustered ground states of Be isotopes. The calculated RMS neutron and matter radii also show a similar trend. The large quadrupole deformation parameter β also supports the presence of 2α-cluster cores with large inter-cluster distances. Moreover, the calculated principal neutron quantum numbers, N_n, of ^{10}Be and ^{14}Be are approximately 4 and 10, respectively, which indicate the $0\hbar\omega$ configuration, whereas for ^{12}Be, $N_n \simeq 8$, which corresponds to the $2\hbar\omega$ configuration.

Tab. 3 Calculated quadrupole deformation parameter β, the RMS proton, neutron, and matter distribution radii of the Be isotopes in the unit of fm, and the principal neutron quantum numbers N_n. The approximated shell model (SM) and molecular orbital (MO) configurations [41] are also listed.

	β	$\sqrt{\langle r_p^2\rangle}$	$\sqrt{\langle r_n^2\rangle}$	$\sqrt{\langle r_m^2\rangle}$	N_n	SM	MO
^{10}Be	0.60	2.44	2.49	2.47	4.03	$0\hbar\omega$	π^2
^{12}Be	0.55	2.57	2.85	2.76	7.60	$2\hbar\omega$	$\pi^2\sigma^2$
^{14}Be	0.60	2.62	2.99	2.88	10.01	$0\hbar\omega$	$\pi^4\sigma^2$

3.2.2 Cluster formation in Be isotopes

Here, I discuss the enhancement of clustering in Be isotopes based on the calculated RWAs. Figure 14(a) shows the calculated α RWA of the ground state of ^{A}Be for the $|\alpha \otimes^{A-4} \mathrm{He}(0_1^+)\rangle$ channel. The amplitudes are suppressed and oscillate in the nuclear interior because of the Pauli exclusion principle. The effect of Pauli exclusion is approximately described by the Wildermuth-Tang rule [42], which asserts that the nodal quantum number n and orbital angular momentum ℓ of the RWA must satisfy the condition $2n+\ell \geq 4$ in ^{10}Be and $2n+\ell \geq 6$ in ^{12}Be and ^{14}Be. Thus, the α RWAs

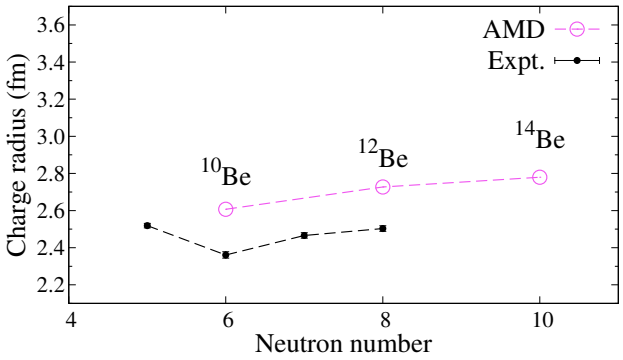

Fig. 13 Calculated RMS charge radii of the Be isotope ground states compared with the experimental charge radii from isotope shift measurements [12–14].

with $\ell = 0$ have two and three nodes in ^{10}Be and ^{12,14}Be, respectively. Note that the condition $2n + \ell \geq 6$ for ^{12}Be implies the dominance of the $2\hbar\omega$ configuration, i.e. the breaking of the $N = 8$ magic number. The amplitudes are peaked at the nuclear exterior ($r \gtrsim 3.0$ fm), indicating the cluster formation at the nuclear surface. The peak position is more outward for ^{12,14}Be than for ^{10}Be, and this result is consistent with the enhanced cluster formation by the excess neutrons occupying the σ orbitals. This trend is also evident from the calculated RMS radius of the RWA, $a_{\rm rms}$, shown in Fig. 15. The $a_{\rm rms}(\alpha)$ of ^{12}Be is larger than that of ^{10}Be owing to the cluster development in ^{12}Be. Additionally, the $a_{\rm rms}(\alpha)$ of ^{14}Be is slightly shorter than that of ^{12}Be, because the two neutrons of ^{14}Be occupying the π orbitals attract the two α particle cores.

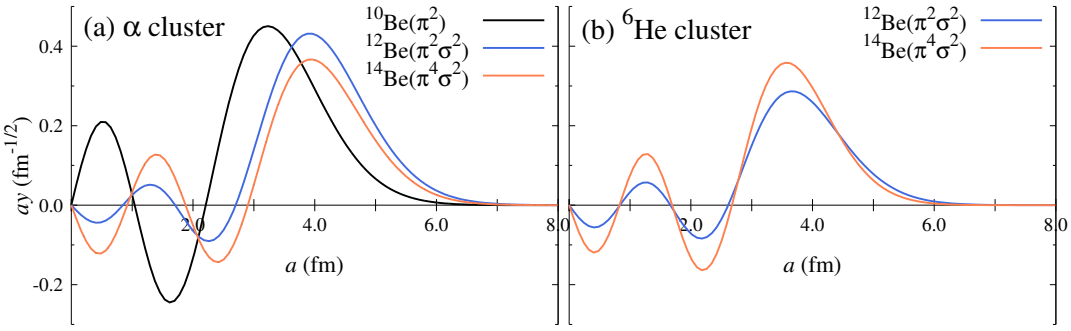

Fig. 14 Calculated α (panel (a)) and ^{6}He (panel (b)) RWAs of the Be isotopes with orbital angular momentum $\ell = 0$.

However, the calculated S-factor for α clustering, shown in Fig. 16, is dependent on the neutron number, which contradicts the aforementioned analysis. The S-factor decreases as the neutron number increases, suggesting the suppression of the α-cluster

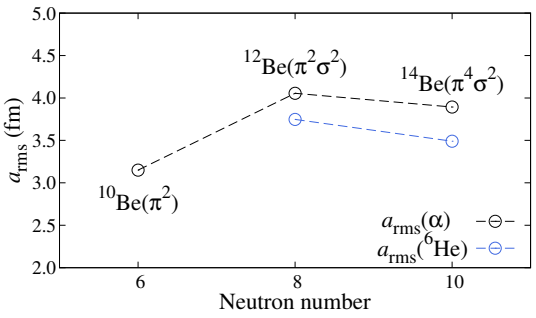

Fig. 15 Calculated RMS radii of the RWAs for α and ^{6}He clusters in the Be isotopes.

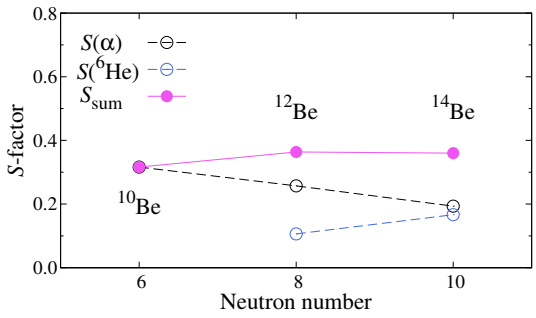

Fig. 16 Calculated α and ^{6}He S-factors and the sum of those S-factors as a function of the neutron number of the Be isotopes.

formation by the excess neutrons. The associated mechanism may be explained as follows: Because of the glue-like role played by the valence neutrons in ^{12}Be, this Be isotope has a mixing of α+^{8}He and ^{6}He+^{6}He configurations. As a result, the $S(\alpha)$ of ^{12}Be becomes smaller than that of ^{10}Be, although the sum of $S(\alpha)$ and $S(^6$He) is larger than that of ^{10}Be. Similarly, ^{14}Be may be an admixture of α+^{10}He and ^{6}He+^{8}He configurations. To verify this hypothesis, the calculated ^{6}He RWAs of ^{12}Be and ^{14}Be are shown in Fig. 14(b) since the ^{6}He RWA of ^{10}Be is equivalent to that of the α RWA. In both ^{12}Be and ^{14}Be, the peak height of the ^{6}He RWA is comparable to that of the α RWA, and the peak position slightly shifts inward, which is reflected by the RMS radii of the RWAs for the α and ^{6}He clusters shown in Fig. 15. Thus, the magnitude of $S(^6$He) is comparable with that of $S(\alpha)$. Here, I assume that the $|\alpha \otimes^{A-4}$ He$\rangle$ and $|^6$He $\otimes^{A-6}$He$\rangle$ channels are not similar to each other in ^{12}Be and ^{14}Be. The sum of $S(\alpha)$ and $S(^6$He), i.e. $S_{\rm sum}$, varies only negligibly with the neutron number. Thus, taking into account the clustering of ^{6}He as well as α, it can be stated that Be isotopes have a well-developed cluster structure. Furthermore, for example in ^{12}Be, $S(\alpha)$ related to the excited state of the residual nucleus, $Y_{\ell=2}[\alpha(0^+) \otimes {}^8\mathrm{He}(2_1^+)]$ channel, is $S(\alpha) \sim 0.15$; $Y_{\ell=4}[{}^6\mathrm{He}(2_1^+) \otimes {}^6\mathrm{He}(2_1^+)]$ channel, is $S(\alpha) \sim 0.23$. The results indicate that the excess neutrons contribute to yield not only α cluster but also ^{6}He cluster, which means that $S(\alpha)$ is not enough to estimate the enhancement of clustering in Be isotopes.

3.3 Cluster formation in B isotopes

3.3.1 Structure of Li isotopes

Table 4 lists the quadrupole deformation parameters β and γ, the RMS proton and neutron distribution radii, the charge radii and those observed radii, and the principal

neutron quantum numbers N_n of Li isotopes. ^{7}Li is expected to have $\alpha + t$ configuration because ^{7}Li is prolately deformed and has one less proton than ^{8}Be which is a famous 2α resonance state having a prolate shape. ^{9}Li is not a very characteristic nucleus while it has a large asymmetry with $N/Z = 2$. N_n of ^{9}Li indicates that all six neutrons are within the $0p$-shell. Different from ^{9}Li, ^{11}Li has interesting properties and is known as a two-neutron halo nucleus. N_n of ^{11}Li indicates that two valence neutrons are in the sd-shell beyond the $N = 8$ shell gap. The calculated intrinsic wave function of ^{11}Li, explained in Appendix B.7, consists of $(1s)^2$ and $(0d)^2$ configurations that amount to 30% and 69%, respectively. Note that this 30% contribution by $(1s)^2$ configuration is close to that of previous works; 33(6)% [43] and 36.8% [44]. Furthermore, the calculated charge radius of ^{11}Li is within an error range of its observed radius. The enhancement of neutrons of ^{11}Li can be seen as the large neutron-skin thickness compared with those ^{7}Li and ^{9}Li, and also the deformation parameters of the proton and neutron with $\beta_p = 0.23$ and $\beta_n = 0.44$, respectively.

Tab. 4 Calculated quadrupole deformation parameters β, γ; the r.m.s. proton and neutron distribution radii and the charge radii and those observed radii [45,46] in the unit of fm; and the principal neutron quantum numbers N_n of Li isotopes.

	β	γ	$\sqrt{\langle r_p^2\rangle}$	$\sqrt{\langle r_n^2\rangle}$	$\sqrt{\langle r_c^2\rangle}$	$\sqrt{\langle r_c^2\rangle}$ (Expt.)	N_n
^{7}Li	0.50	2	2.18	2.31	2.36	2.39(3)	2.01
^{9}Li	0.55	29	2.24	2.45	2.42	2.217(35)	4.02
^{11}Li	0.39	6	2.31	2.77	2.49	2.467(37)	8.00

3.3.2 Structure of B isotopes

Although the structures of B isotopes have been theoretically studied by many authors [10, 25–27, 47, 48], the physical quantities, which directly indicate clustering, have not been discussed in detail. Here, I explain the calculated ground-state properties of B isotopes. The calculated spin-parity of the ground states of ^{11,13,15,17,19}B are $J^\pi = 3/2^-$, which is consistent with the experimental data. Table 5 lists the calculated quadrupole deformation parameters β and γ, and the RMS proton, neutron, and matter distribution radii of the B isotopes. The principal neutron quantum numbers, N_n, are approximately 4, 6, 10, 14, and 18 for ^{11,13,15,17,19}B, respectively, which indicate that all the B isotopes are dominated by the $0\hbar\omega$ configurations. The deformation parameters γ show that ^{13}B, ^{15}B, and ^{17}B are prolately deformed, while ^{11}B and ^{19}B are oblately deformed. Remarkably, in the present calculations, ^{19}B is oblately deformed ($\gamma_{p,n} \approx 60^\circ$), while the spin-fixed AMD calculations [27] yielded a prolate deformation. Figure 18 shows the energies of before (after) projected model wave functions, Eq. (2.11), of ^{19}B onto the $3/2^-$ state as a function of the quadrupole

deformation parameter β as an open (a filled) circle. Prolately deformed wave functions of ^{19}B are also described but those energies are larger than that of oblate deformation. This difference significantly affects the cluster formation probabilities as discussed later in this paper. Figure 17 shows the calculated RMS point proton radii, which are in reasonable agreement with the experimental values, except for ^{11}B. The magnetic moments μ and electric quadrupole moments Q_p of $^{11-17}$B shown in Figs. 19 and 20 are also in good agreement with the observed values and do not exhibit a strong dependence on the neutron number. Thus, the present calculation results successfully describe the ground states of B isotopes.

Tab. 5 Calculated deformation parameters β, γ; the RMS proton, neutron, and matter distribution radii; the principal neutron quantum numbers N_n of the B isotope ground states. The γ values and radii are given in the unit of degree and fm, respectively.

	β	γ	$\sqrt{\langle r_p^2 \rangle}$	$\sqrt{\langle r_n^2 \rangle}$	$\sqrt{\langle r_m^2 \rangle}$	N_n
^{11}B	0.45	59	2.45	2.49	2.47	4.03
^{13}B	0.30	6	2.47	2.56	2.52	6.04
^{15}B	0.50	0	2.61	2.87	2.79	10.00
^{17}B	0.55	9	2.66	3.02	2.92	14.01
^{19}B	0.45	60	2.69	3.12	3.01	18.01

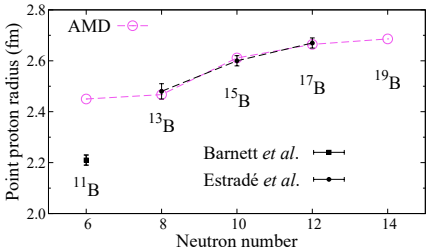

Fig. 17 Calculated RMS point proton radii of the B isotopes compared with the observed values [49, 50].

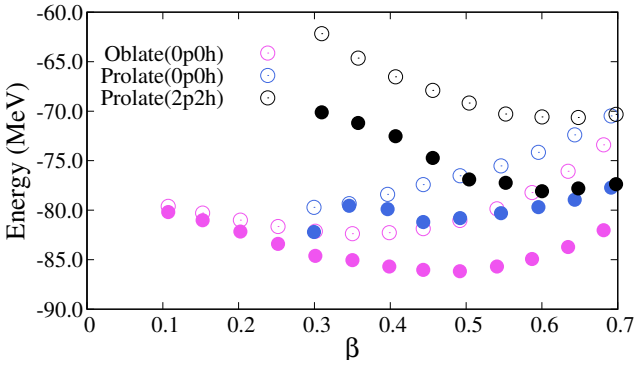

Fig. 18 Energies of before (after) projected model wave functions of ^{19}B onto $3/2^-$ state as a function of the quadrupole deformation parameter β are shown as an open (a filled) circle.

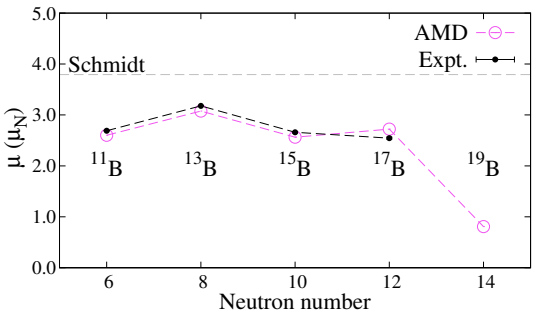

Fig. 19 Calculated magnetic moments μ of the B isotope ground states compared with the observed values [51–54]. The gray dashed line shows the Schmidt value for the $p_{3/2}$ proton.

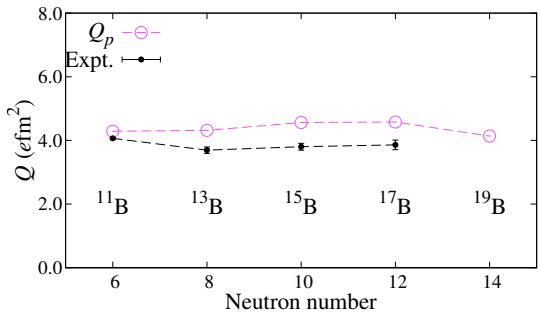

Fig. 20 Calculated electric quadrupole moments Q_p of the B isotope ground states compared with the observed values [55–57].

3.3.3 Cluster formation in B isotopes

In this subsection, I discuss the cluster formation in B isotopes based on the intrinsic density distributions, RWAs, radii of the RWAs, and S-factors.

Cluster formation in B isotopes can be evaluated from Fig. 21, which shows the proton, neutron, and matter intrinsic density distributions of the Be and B isotopes. The peak positions of the proton density distributions are marked by points, and the distance d between them are shown in panel (c). All the Be isotopes exhibit a prolate shape, and the distance d increases as the neutron number increases, which is consistent with the growth of clustering toward the neutron drip-line. For the B isotopes, the S-factors are expected to be smaller than those of the Be isotopes, because the distance d is smaller than that of the Be isotopes. The S-factor increases as a function of the neutron number until ^{17}B. The isotope ^{19}B has an oblate shape and does not exhibit clustered structures. Thus, I expect that the clustering is enhanced until ^{17}B, but the corresponding S-factors are always smaller than those of the Be isotopes.

Next, I discuss the RWAs in the $|\alpha\otimes^{A-4}\mathrm{Li}(3/2^-_1)\rangle$ channel with $A = 11$, 13, and 15 as shown in Fig. 22(a). I assume that the $N = 8$ magic number is broken in ^{11}Li and the last neutrons occupy the $1s$ and $0d$ orbits which amount to 30% and 70%, respectively. The RWAs of the B isotopes are peaked at the nuclear exterior and suppressed in the interior due to the Pauli exclusion satisfying the Wildermuth-Tang rule [42]. The peak height is much smaller than that of the Be isotopes, suggesting the presence of less developed clustered structures as expected. Similar to the case of Be and C isotopes [23], the $S(\alpha)$ decreases as the neutron number increases as shown

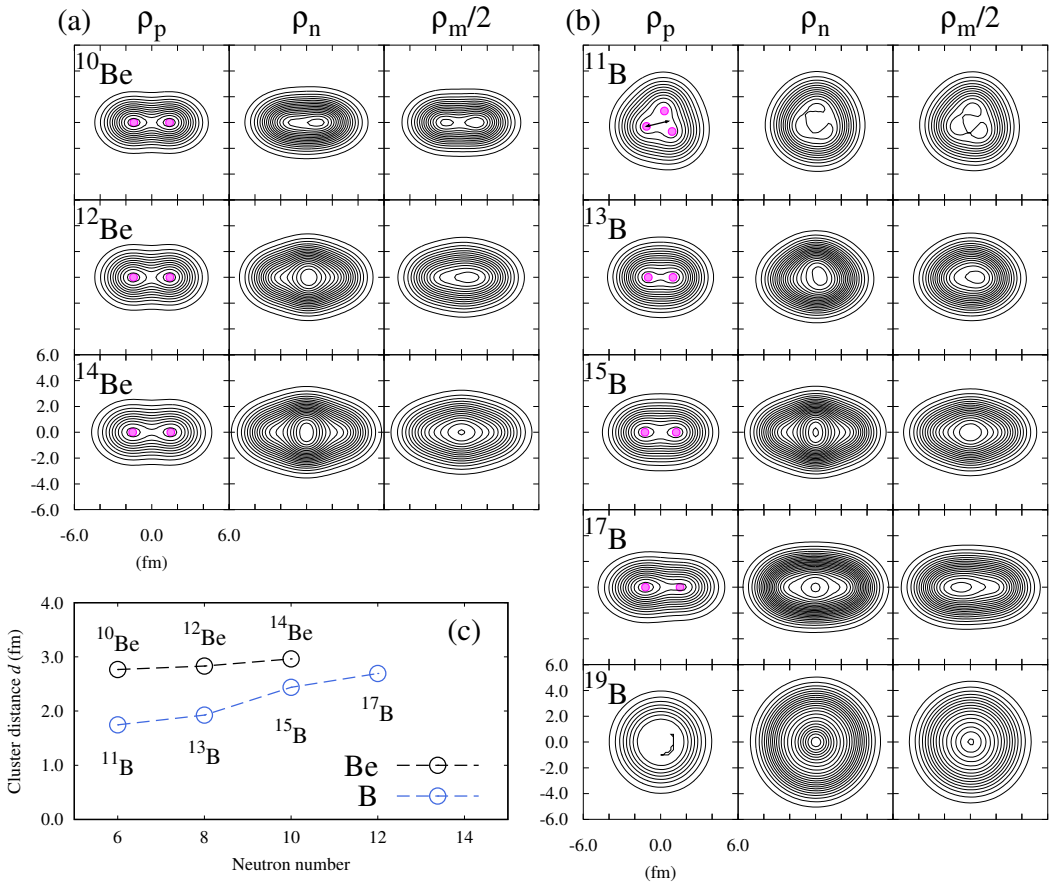

Fig. 21 Panels (a) and (b) show the proton, neutron, and matter intrinsic density of Be and B isotopes, respectively. The peak positions of the proton density are marked with a point and those distances are shown in panel (c). Note for ^{11}B that the largest distance between a peak and the mean position of the other peaks is adopted and shown as an arrow.

in Fig. 23 because of the excess neutrons, which cause the mixing of the α+^{9}Li and ^{6}He+^{7}Li configurations in ^{13}B and that of the ^{6}He+^{9}Li and ^{8}He+^{7}Li configurations in ^{15}B. The calculated ^{6}He and ^{8}He RWAs are shown in Figs. 22(b) and (c), respectively. Evidently, in ^{13}B, the peak height of the ^{6}He RWA is comparable to that of the α RWA. In ^{15}B, the peak heights of the ^{6}He and ^{8}He RWAs are larger than that of α. Similarly, the excess neutrons in ^{17}B contribute to the formation of the ^{8}He+^{9}Li

configuration. These features are reflected in the S-factors depicted in Fig. 23 as well as the radii of the RWAs shown in Fig. 24. Clearly, some of the α, ^{6}He, and ^{8}He cluster structures are enhanced in ^{11,13,15,17}B. In Fig. 23, $S_{\rm sum}$ shows the sum of $S(\alpha)$, $S(^6\mathrm{He})$, and $S(^8\mathrm{He})$ and is not hindered by the excess neutrons in the isotopes up to ^{17}B.

In ^{19}B, the corresponding RWA and S-factor indicate a less developed ^{8}He cluster structure, which is expected from the intrinsic densities. Therefore, the behavior of $S_{\rm sum}$ is consistent with the enhancement of clustering, determined from the intrinsic density distributions in Fig. 21 showing a certain amount of cluster development with smaller $S_{\rm sum}$ values compared with that of Be isotopes. This result indicates that ^{6}He and ^{8}He clusters as well as α clusters are exhibited due to the excess neutrons in B isotopes.

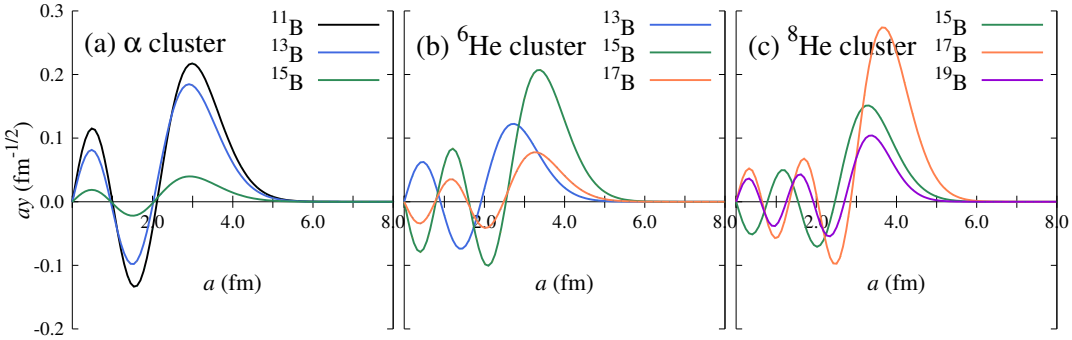

Fig. 22 Calculated α (panel (a)), ^{6}He (panel (b)), and ^{8}He (panel (c)) RWAs of the B isotopes with orbital angular momentum $\ell = 0$.

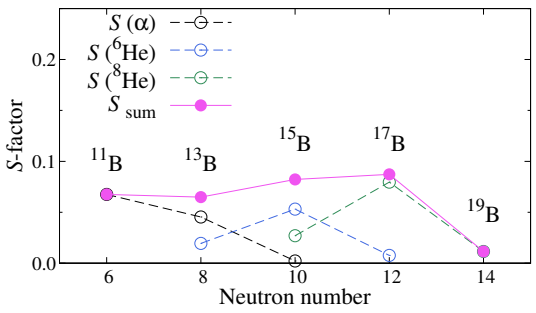

Fig. 23 Calculated α, ^{6}He, and ^{8}He S-factors and the sum of those S-factors as a function of the neutron number of the B isotopes.

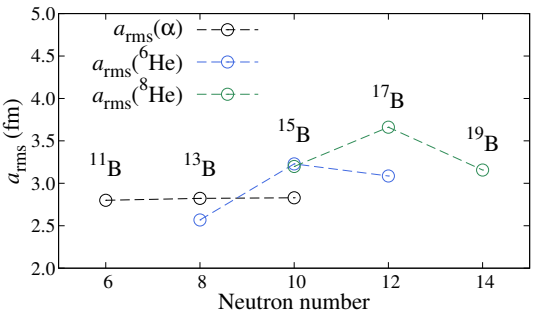

Fig. 24 Calculated RMS radii of the RWAs for α, ^{6}He, and ^{8}He clusters of the B isotopes.

Here, I also discuss the cluster formation in ^{11}B which has an oblate shape with

three peaks in the distributions of proton $\rho_{\rm p}$ and neutron $\rho_{\rm n}$ (Fig. 21). Thus, it is expected that two excess neutrons of ^{11}B are in the vicinity of a single proton forming t and therefore ^{11}B is expected to have a $\alpha+\alpha+t$ configuration. Addition to the α cluster formation in Fig. 22(a) and Fig. 23, t RWA and its S-factor are shown in Fig. 25 and Tab. 6, respectively. The peak position of the α and t RWAs are close to each other with the almost same amplitudes. The calculated t S-factor, $S(t)=0.11$, is comparable to $S(\alpha)=0.07$. Thus, in ^{11}B, α and t clusters emerge with approximately the same degree of clustering. Table 6 also lists the $S(\alpha)$ in ^{12}C and ^{14}C calculated by the same framework [23]. ^{12}C is 3α system and is composed of one more proton than ^{11}B. ^{14}C is composed of two more neutrons than 3α system of ^{12}C. $S(\alpha)$ in ^{14}C is much reduced to approximately 1/3 of the ^{12}C, but is largest among the neutron-rich C isotopes and is comparable to the $S(\alpha)$ and $S(t)$ in ^{11}B. This indicates that the $S(\alpha)$ and $S(t)$ in ^{11}B are not small because those S-factors are comparable to the $S(\alpha)$ in ^{14}C although the $S(\alpha)$ is reduced when a nucleon is added to the 3α system. Therefore, ^{11}B is still keeping the $\alpha+\alpha+t$ structure, which seems to support the previous study [58].

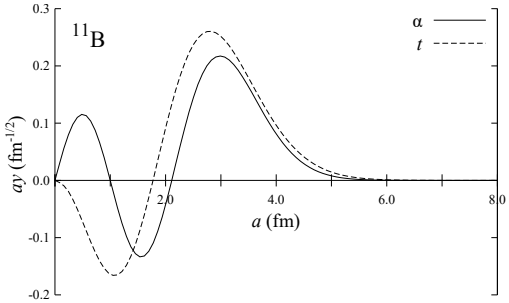

Fig. 25 Calculated α and t RWAs of ^{11}B with orbital angular momentum $\ell=0$ and $\ell=1$, respectively.

Tab. 6 Calculated α and t S-factors of ^{11}B are compared with the α S-factors of ^{12}C and ^{14}C calculated in Ref. [23].

	channel	S-factor
^{11}B	$Y_{\ell=0}[\alpha(0^+)\otimes{}^7\mathrm{Li}(\frac{3}{2}^-)]$	0.07
^{11}B	$Y_{\ell=1}[t(\frac{1}{2}^+)\otimes{}^8\mathrm{Be}(0^+)]$	0.11
^{12}C	$Y_{\ell=0}[\alpha(0^+)\otimes{}^8\mathrm{Be}(0^+)]$	0.30
^{14}C	$Y_{\ell=0}[\alpha(0^+)\otimes{}^{10}\mathrm{Be}(0^+)]$	0.10

4 Summary

Cluster formation is a universal phenomenon exhibited at all levels constituting the hierarchy of matter. Notably, in finite nuclei, cluster formation is expected to be hindered by the growth of a neutron skin. Recently, it was shown that the proton-induced α knockout reaction (p, $p\alpha$) is useful for assessing the α cluster formation at the nuclear surface. Using this reaction, the negative correlation between the neutron-skin thickness and the α cluster formation at the nuclear surface of Sn isotopes has been reported. On the other hand, the α cluster formation in Be and B isotopes is predicted to enhance as the neutron drip-line approaches. However, this prediction was not based on the physical quantity which can directly probe the α cluster structure. Thus, I theoretically evaluated the α cluster formation by the α S-factors in neutron-rich Be and B isotopes to clarify the possible clustering toward the neutron drip-line using the AMD+RWA framework. Additionally, considering the excess neutrons surrounding the two α cores in Be and B isotopes, ^{6}He and ^{8}He clusters were also evaluated. In this study, the ground-state Φ_A(g.s.) to the ground-state Φ_{A-C_1}(g.s.) channel of C_1 cluster formation was only evaluated, which can be measured by the (p, $p\alpha$) reaction in the case of $C_1 = \alpha$.

The AMD framework successfully described the ground-state properties of both the Be and B isotope chains. I estimated the cluster formation from the intrinsic density distributions and the proton distribution radii in the Be and B isotopes as well as by referring to the molecular orbital model for the Be isotopes. Although the calculated α spectroscopic factors, i.e. $S(\alpha)$, show a negative correlation with the neutron number, the sum of $S(\alpha)$ and $S(^6\mathrm{He})$ for the Be isotopes and that of $S(\alpha)$, $S(^6\mathrm{He})$, and $S(^8\mathrm{He})$ for the B isotopes are not being hindered as the neutron drip-line approaches except for ^{19}B. This result is consistent with the clustering estimated from the intrinsic density distributions. Thus, the results of this study revealed the possibility of cluster formation as the neutron drip-line is approached in Be and B isotopes, by explaining the mechanism of cluster formation for the former and showing consistency between the cluster distances of the intrinsic density distributions and cluster formation for the latter. Additionally, t spectroscopic factor in ^{11}B was microscopically calculated and it was comparable to that of α cluster, which may support the $\alpha + \alpha + t$ model.

It can be concluded that the excess neutrons surrounding α cores contribute to yield ^{6}He and ^{8}He clusters as well as α clusters. The decrease in α spectroscopic factor toward the neutron drip-line in Be and B isotopes is due to considering only the ground state of the residual nuclei, meaning that it does not indicate that α cluster formation is not increased. Namely, $S(\alpha)$ is not enough to estimate the enhancement of clustering in neutron-rich Be and B isotopes.

Appendix A AMD wave function

A.1 Decomposition of the center-of-mass coordinate

The AMD wave function Eq. (2.3) can be decomposed into the internal wave function $\Phi_{\rm int}$ and the center-of-mass wave function $\Phi_{\rm cm}$:

$$\Phi_{\rm AMD} = \Phi_{\rm int}\Phi_{\rm cm}, \tag{A.1}$$

$$\Phi_{\rm int} = \frac{1}{\sqrt{A!}} \begin{vmatrix} \varphi_1(\boldsymbol{r}'_1) & \cdots & \varphi_A(\boldsymbol{r}'_1) \\ \vdots & \ddots & \vdots \\ \varphi_1(\boldsymbol{r}'_A) & \cdots & \varphi_A(\boldsymbol{r}'_A) \end{vmatrix}, \tag{A.2}$$

$$\widetilde{\Phi}_{\rm cm} = \prod_{\sigma=x,y,z} \left(\frac{2A\nu_\sigma}{\pi}\right)^{1/4} \exp\{-A\nu_\sigma r^2_{{\rm cm},\sigma}\} = \Phi_{\rm cm} \prod_{\sigma=x,y,z} \left(\frac{2A\nu_\sigma}{\pi}\right)^{1/4}, \tag{A.3}$$

where $\widetilde{\Phi}_{\rm cm}$ is renormalized. Using the relation $r'_{i\sigma} = r_{i\sigma} - r_{{\rm cm},\sigma}$, the spatial part of the single particle wave function Eq. (2.5) can be written as,

$$\phi_i(\boldsymbol{r}) = \prod_{\sigma=x,y,z} \left(\frac{2\nu_\sigma}{\pi}\right)^{1/4} \exp\{-\nu_\sigma(r_{i\sigma} - Z_{i\sigma})\}^2, \tag{A.4}$$

$$= \prod_{\sigma=x,y,z} \left(\frac{2\nu_\sigma}{\pi}\right)^{1/4} \exp\{-\nu_\sigma(r'_{i\sigma} + r_{{\rm cm},\sigma} - Z_{i\sigma})\}^2, \tag{A.5}$$

$$= \phi_i(\boldsymbol{r}') \prod_{\sigma=x,y,z} \exp\{-\nu_\sigma r^2_{{\rm cm},\sigma}\} \exp\{-2\nu_\sigma r_{{\rm cm},\sigma}(r'_{i\sigma} - Z_{i\sigma})\}. \tag{A.6}$$

Inserting this equation into the AMD wave function Eq. (2.3), the center-of-mass coordinate can be separated:

$$\Phi_{\rm AMD} = \Phi_{\rm int} \prod_{i=1}^{A} \prod_{\sigma=x,y,z} \exp\{-\nu_\sigma r^2_{{\rm cm},\sigma}\} \exp\{-2\nu_\sigma r_{{\rm cm},\sigma}(r'_{i\sigma} - Z_{i\sigma})\}, \tag{A.7}$$

$$= \Phi_{\rm int} \exp\left\{-\sum_{i=1}^{A} \sum_{\sigma=x,y,z} \nu_\sigma r^2_{{\rm cm},\sigma}\right\} \exp\left\{-\sum_{\sigma=x,y,z} 2\nu_\sigma r_{{\rm cm},\sigma} \left(\sum_{i=1}^{A} r'_{i\sigma}\right)\right\}$$
$$\times \exp\left\{\sum_{\sigma=x,y,z} 2\nu_\sigma r_{{\rm cm},\sigma} \left(\sum_{i=1}^{A} Z_{i\sigma}\right)\right\}, \tag{A.8}$$

$$= \Phi_{\rm int} \exp\left\{-A \sum_{\sigma=x,y,z} \nu_\sigma r^2_{{\rm cm},\sigma}\right\} = \Phi_{\rm int}\Phi_{\rm cm}, \tag{A.9}$$

where the relative coordinate $r'_{i\sigma}$ satisfies the relation $\sum_{i=1}^{A} r'_{i\sigma} = 0$. Furthermore, it is imposed that $\sum_{i=1}^{A} Z_{i\sigma} \equiv 0$ without the loss of generality.

A.2 Expectation values

Single particle wave packet

$$\varphi_i(\boldsymbol{r}) = \phi_i(\boldsymbol{r})\chi_i\eta_i, \tag{A.10}$$

$$\phi_i(\boldsymbol{r}) = \prod_{\sigma=x,y,z}\left(\frac{2\nu_\sigma}{\pi}\right)^{1/4}\exp\left\{-\nu_\sigma(r_\sigma - Z_{i\sigma})\right\}^2. \tag{A.11}$$

Overlap

The matrix element B_{ij} of an $A\times A$ overlap matrix B is defined as,

$$B_{ij} \equiv \langle\varphi_i|\varphi_j\rangle = D_{ij}S_{ij}\delta_{\alpha\beta} \tag{A.12}$$

$$D_{ij} \equiv \langle\phi_i|\phi_j\rangle = \int \mathrm{d}\boldsymbol{r}\ \phi_i^*(\boldsymbol{r})\phi_j(\boldsymbol{r}), \tag{A.13}$$

$$S_{ij} \equiv \langle\chi_i|\chi_j\rangle = a_i^*a_j + b_i^*b_j, \tag{A.14}$$

$$\delta_{\alpha\beta} \equiv \langle\eta_\alpha|\eta_\beta\rangle. \tag{A.15}$$

Here, I derive the kernel D_{ij}. The integrand is given as,

$$\phi_i^*(r_\sigma)\phi_j(r_\sigma) = \left(\tfrac{2\nu_\sigma}{\pi}\right)^{1/2}\exp\left[-\nu_\sigma\left\{(r_\sigma - Z_{i\sigma}^*)^2 + (r_\sigma - Z_{j\sigma})^2\right\}\right], \tag{A.16}$$

$$= \left(\tfrac{2\nu_\sigma}{\pi}\right)^{1/2} e^{-\frac{\nu_\sigma}{2}(Z_{i\sigma}^* - Z_{j\sigma})^2}\exp\{-2\nu_\sigma(r_\sigma - Z_{ij\sigma})^2\}, \tag{A.17}$$

$$= \left(\tfrac{2\nu_\sigma}{\pi}\right)^{1/2} D_{ij\sigma}\exp\{-2\nu_\sigma(r_\sigma - Z_{ij\sigma})^2\}, \tag{A.18}$$

$$Z_{ij\sigma} \equiv (Z_{i\sigma}^* + Z_{j\sigma})/2. \tag{A.19}$$

Thus,

$$D_{ij} = \prod_\sigma\left(\tfrac{2\nu_\sigma}{\pi}\right)^{1/2} e^{-\frac{\nu_\sigma}{2}(Z_{i\sigma}^* - Z_{j\sigma})^2}\int \mathrm{d}r_\sigma\ \exp\{-2\nu_\sigma(r_\sigma - Z_{ij\sigma})^2\}, \tag{A.20}$$

$$= \boxed{\prod_{\sigma=x,y,z}\exp\left\{-\frac{\nu_\sigma}{2}(Z_{i\sigma}^* - Z_{j\sigma})^2\right\}}. \tag{A.21}$$

One-body operator

One-body operator $\hat{\mathcal{O}}$ is defied as $\hat{\mathcal{O}} \equiv \sum_{i=1}^A o_i$, and its expectation value is given by,

$$\langle\hat{\mathcal{O}}\rangle = \langle\Phi_{\mathrm{int}}|\hat{\mathcal{O}}|\Phi_{\mathrm{int}}\rangle = \sum_\alpha\sum_{ij\in\alpha}\langle\varphi_i|\hat{o}|\varphi_j\rangle(B^{-1})_{ji}. \tag{A.22}$$

◦ *Kinetic energy*

The kinetic energy and its expectation value are given by,

$$\hat{\mathcal{T}} = \sum_{i=1}^{A} \frac{-\hbar^2}{2m} \boldsymbol{\nabla}_i^2 = \sum_{i=1}^{A} \hat{t}_i, \tag{A.23}$$

$$\langle \hat{\mathcal{T}} \rangle = -\frac{\hbar^2}{2m} \sum_{\alpha} \sum_{ij \in \alpha} \langle \varphi_i | \boldsymbol{\nabla}^2 | \varphi_j \rangle (B^{-1})_{ji}, \tag{A.24}$$

$$= -\frac{\hbar^2}{2m} \sum_{\alpha} \sum_{ij \in \alpha} S_{ij} \langle \phi_i | \boldsymbol{\nabla}^2 | \phi_j \rangle (B^{-1})_{ji}, \tag{A.25}$$

Using these relations:

$$\nabla_\tau \phi_j(\boldsymbol{r}) = -2\nu_\tau (r_\tau - Z_{j\tau}) \phi_j(\boldsymbol{r}), \tag{A.26}$$

$$\nabla_\tau^2 \phi_j(\boldsymbol{r}) = \{-2\nu_\tau + 4\nu_\tau^2 (r_\tau - Z_{j\tau})^2\} \phi_j(\boldsymbol{r}), \tag{A.27}$$

$$\phi_i^*(\boldsymbol{r}) \phi_j(\boldsymbol{r}) = D_{ij} \prod_\sigma \left(\tfrac{2\nu_\sigma}{\pi}\right)^{1/2} \exp\{-2\nu_\sigma (r_\sigma - Z_{ij\sigma})^2\} \tag{A.28}$$

$$\begin{aligned} \therefore \phi_i^*(\boldsymbol{r}) \nabla_\tau^2 \phi_j(\boldsymbol{r}) = {} & \{-2\nu_\tau + 4\nu_\tau^2 (r_\tau - Z_{j\tau})^2\} \\ & \times D_{ij} \prod_\sigma \left(\tfrac{2\nu_\sigma}{\pi}\right)^{1/2} \exp\{-2\nu_\sigma (r_\sigma - Z_{ij\sigma})^2\}, \end{aligned} \tag{A.29}$$

the kernel is obtained as,

$$\langle \phi_i | \nabla_\tau^2 | \phi_j \rangle = \int \mathrm{d}\boldsymbol{r}\ \phi_i^*(\boldsymbol{r}) \nabla_\tau^2 \phi_j(\boldsymbol{r}), \tag{A.30}$$

$$= D_{ij} \{-\nu_\tau + \nu_\tau^2 (Z_{i\tau}^* - Z_{j\tau})^2\}, \tag{A.31}$$

$$\therefore \langle \phi_i | \boldsymbol{\nabla}^2 | \phi_j \rangle = D_{ij} \sum_\tau \{-\nu_\tau + \nu_\tau^2 (Z_{i\tau}^* - Z_{j\tau})^2\}. \tag{A.32}$$

Thus, the kinetic energy is given by,

$$\langle \hat{\mathcal{T}} \rangle = -\frac{\hbar^2}{2m} \sum_{\alpha} \sum_{ij \in \alpha} S_{ij} D_{ij} (B^{-1})_{ji} \sum_\tau \{-\nu_\tau + \nu_\tau^2 (Z_{i\tau}^* - Z_{j\tau})^2\}, \tag{A.33}$$

$$= \boxed{\frac{\hbar^2}{2m} \sum_{\tau=x,y,z} \left\{ A\nu_\tau - \sum_{\alpha} \sum_{ij \in \alpha} B_{ij} (B^{-1})_{ji} \nu_\tau^2 (Z_{i\tau}^* - Z_{j\tau})^2 \right\}}. \tag{A.34}$$

◦ *Kinetic energy of CoM*

The operator for the center-of-mass kinetic energy, $\hat{t}_{\mathrm{cm}}$, acts only on the center-

of-mass wave function $\Phi_{\rm cm}$:

$$\langle \hat{t}_{\rm cm} \rangle = \langle \Phi_{\rm AMD} | \hat{t}_{\rm cm} | \Phi_{\rm AMD} \rangle, \tag{A.35}$$

$$= \langle \Phi_{\rm int} | \Phi_{\rm int} \rangle \langle \widetilde{\Phi}_{\rm cm} | \hat{t}_{\rm cm} | \widetilde{\Phi}_{\rm cm} \rangle = \langle \widetilde{\Phi}_{\rm cm} | \hat{t}_{\rm cm} | \widetilde{\Phi}_{\rm cm} \rangle, \tag{A.36}$$

$$\hat{t}_{\rm cm} = \sum_{i=1}^{A} \frac{-\hbar^2}{2(Am)} \boldsymbol{\nabla}^2_{{\rm cm},i}. \tag{A.37}$$

The kernel is obtained as the simple formula,

$$\nabla_{{\rm cm},\tau} \widetilde{\Phi}_{\rm cm}(\boldsymbol{r}_{\rm cm}) = -2A\nu_\tau r_{{\rm cm},\tau} \widetilde{\Phi}_{\rm cm}(\boldsymbol{r}_{\rm cm}), \tag{A.38}$$

$$\nabla^2_{{\rm cm},\tau} \widetilde{\Phi}_{\rm cm}(\boldsymbol{r}_{\rm cm}) = (-2A\nu_\tau + 4A^2\nu_\tau^2 r_{{\rm cm},\tau}) \widetilde{\Phi}_{\rm cm}(\boldsymbol{r}_{\rm cm}), \tag{A.39}$$

$$\therefore \langle \widetilde{\Phi}_{\rm cm}(\boldsymbol{r}_{\rm cm}) | \boldsymbol{\nabla}^2_{\rm cm} | \widetilde{\Phi}_{\rm cm}(\boldsymbol{r}_{\rm cm}) \rangle = -A \sum_\tau \nu_\tau. \tag{A.40}$$

Thus, the center-of-mass kinetic energy is given by,

$$\langle \hat{t}_{\rm cm} \rangle = -\frac{\hbar^2}{2Am} \sum_{i=1}^{A} \langle \widetilde{\Phi}_{\rm cm}(\boldsymbol{r}_{\rm cm}) | \boldsymbol{\nabla}^2_{\rm cm} | \widetilde{\Phi}_{\rm cm}(\boldsymbol{r}_{\rm cm}) \rangle = \boxed{\frac{\hbar^2}{2m} \sum_{\tau=x,y,z} \nu_\tau}. \tag{A.41}$$

◦ *Density distribution*

The intrinsic density operator and its expectation value are given by,

$$\hat{\rho}(\boldsymbol{R}) = \sum_{i=1}^{A} \delta(\boldsymbol{r}_i - \boldsymbol{R}), \tag{A.42}$$

$$\langle \hat{\rho}(\boldsymbol{R}) \rangle = \sum_\alpha \sum_{ij\in\alpha} S_{ij} \langle \phi_i(\boldsymbol{r}) | \delta(\boldsymbol{r} - \boldsymbol{R}) | \phi_j(\boldsymbol{r}) \rangle (B^{-1})_{ji}, \tag{A.43}$$

$$= \sum_\alpha \sum_{ij\in\alpha} S_{ij} (B^{-1})_{ji} \int {\rm d}\boldsymbol{r}\ \delta(\boldsymbol{r} - \boldsymbol{R}) \phi_i^*(\boldsymbol{r}) \phi_j(\boldsymbol{r}), \tag{A.44}$$

$$= \sum_\alpha \sum_{ij\in\alpha} S_{ij} (B^{-1})_{ji} \phi_i^*(\boldsymbol{R}) \phi_j(\boldsymbol{R}), \tag{A.45}$$

$$= \boxed{\sum_\alpha \sum_{ij\in\alpha} B_{ij} (B^{-1})_{ji} \prod_\sigma \left(\tfrac{2\nu_\sigma}{\pi}\right)^{1/2} \exp\{-2\nu_\sigma (r_\sigma - Z_{ij\sigma})^2\}}. \tag{A.46}$$

◦ *RMS radius*

The RMS radius operator and its expectation value are given by,

$$\hat{r}^2 = \frac{1}{A} \sum_{i=1}^{A} \boldsymbol{r}_i^2, \tag{A.47}$$

$$\langle \hat{r}^2 \rangle = \frac{1}{A} \sum_\alpha \sum_{ij\in\alpha} S_{ij} \langle \phi_i | \boldsymbol{r}^2 | \phi_j \rangle (B^{-1})_{ji}, \tag{A.48}$$

$$\langle\phi_i|\hat{r}_\tau^2|\phi_j\rangle = \int \mathrm{d}\boldsymbol{r}\ \phi_i^*(\boldsymbol{r}) r_\tau^2 \phi_j(\boldsymbol{r}) = D_{ij}\frac{1}{4\nu_\tau}\{1+\nu_\tau(Z_{i\tau}^* + Z_{j\tau})^2\}, \tag{A.49}$$

$$\langle\hat{r}^2\rangle = \frac{1}{A}\sum_\alpha \sum_{ij\in\alpha}\sum_\tau B_{ij}(B^{-1})_{ji}\frac{1}{4\nu_\tau}\{1+\nu_\tau(Z_{i\tau}^* + Z_{j\tau})^2\}, \tag{A.50}$$

$$= \boxed{\sum_{\tau=x,y,z}\frac{1}{4\nu_\tau}\left\{1+\frac{1}{A}\sum_\alpha\sum_{ij\in\alpha}B_{ij}(B^{-1})_{ji}\nu_\tau(Z_{i\tau}^* + Z_{j\tau})^2\right\}}. \tag{A.51}$$

◦ *Principal quantum number*

The number operator $\hat{N}_{\sigma\tau}$ is defined as,

$$\hat{N}_{\sigma\tau} = \sum_{i=1}^{A}\hat{n}_{\sigma\tau}, \tag{A.52}$$

$$\hat{n}_{\sigma\tau} = \hat{a}_\sigma^\dagger \hat{a}_\tau, \quad \hat{a}_\sigma^\dagger = \hat{r}_\sigma + \frac{\hat{p}_\sigma}{2i\hbar\nu_\sigma}, \quad \hat{a}_\sigma = \hat{r}_\sigma - \frac{\hat{p}_\sigma}{2i\hbar\nu_\sigma}, \tag{A.53}$$

$$\hat{p}_\sigma = -i\hbar\nabla_\sigma, \tag{A.54}$$

where $\hat{p}_\sigma$ is a momentum operator. The operator $\hat{a}_\sigma$ satisfies the relation,

$$\hat{a}_\sigma\phi(\boldsymbol{r}) = Z_\sigma\phi(\boldsymbol{r}). \tag{A.55}$$

Thus, the principal quantum number is given by,

$$\hat{N}_{\sigma\tau} = \sum_\alpha\sum_{ij\in\alpha} S_{ij}\langle\phi_i|\hat{n}_{\sigma\tau}|\phi_j\rangle(B^{-1})_{ji}, \tag{A.56}$$

$$= \boxed{\sum_\alpha\sum_{ij\in\alpha} Z_{i\sigma}^* Z_{j\tau} B_{ij}(B^{-1})_{ji}}. \tag{A.57}$$

Two-body operator

Two-body operator is defied as $\hat{\mathcal{O}} \equiv \sum_{ij=1}^{A}\hat{o}_{ij}$, and its expectation value is given by,

$$\langle\hat{\mathcal{O}}\rangle = \sum_\alpha\sum_\beta\sum_{ij\in\alpha}\sum_{ij\in\beta}\langle\varphi_i\varphi_j|\hat{o}|\varphi_k\varphi_\ell - \varphi_\ell\varphi_k\rangle(B^{-1})_{ki}(B^{-1})_{\ell j}. \tag{A.58}$$

◦ *Central potential*

The central potential is given in a Gaussian form,

$$\hat{\mathcal{V}} = \frac{1}{2}\sum_{ij=1}^{A} X e^{-a\boldsymbol{r}_{ij}^2} = \frac{1}{2}\sum_{ij=1}^{A}\hat{v}_{ij}, \quad \boldsymbol{r}_{ij} = \boldsymbol{r}_i - \boldsymbol{r}_j, \tag{A.59}$$

$$\hat{X} = W + B\hat{P}_\sigma - H\hat{P}_\tau - M\hat{P}_\sigma\hat{P}_\tau, \tag{A.60}$$

Using the relations Eq. (A.28), the integrand is obtained as,

$$\begin{aligned}&\phi_i^*(\boldsymbol{r_1})\phi_j^*(\boldsymbol{r_2})\phi_k(\boldsymbol{r_1})\phi_\ell(\boldsymbol{r_2})\\&\qquad = D_{ik}D_{j\ell}\prod_\sigma \tfrac{2\nu_\sigma}{\pi} e^{-4\nu_\sigma\left(R_\sigma-\frac{1}{4}Z^{(+)}_{ijk\ell,\sigma}\right)^2} e^{-\nu_\sigma\left(r_\sigma-\frac{1}{2}Z^{(-)}_{ijk\ell,\sigma}\right)^2},\end{aligned} \tag{A.61}$$

where $\boldsymbol{Z}^{(\pm)}_{ijk\ell} \equiv 2(\boldsymbol{Z}_{ik} \pm \boldsymbol{Z}_{j\ell})$ and $\boldsymbol{R} = \frac{1}{2}(\boldsymbol{r}_1 + \boldsymbol{r}_2)$. The integration over $\boldsymbol{R}$ can easily performed:

$$\int \mathrm{d}\boldsymbol{R}\, \phi_i^*(\boldsymbol{r}_1)\phi_j^*(\boldsymbol{r}_2)\phi_k(\boldsymbol{r}_1)\phi_\ell(\boldsymbol{r}_2) = D_{ik}D_{j\ell}\prod_\sigma \left(\tfrac{\nu_\sigma}{\pi}\right)^{1/2} e^{-\nu_\sigma\left(r_\sigma-\frac{1}{2}Z^{(-)}_{ijk\ell,\sigma}\right)^2}. \tag{A.62}$$

The Eq. (A.58) for the central potential is written as,

$$\langle\hat{\mathcal{V}}\rangle = \frac{1}{2}\sum_{\alpha\beta}\sum_{ij\in\alpha}\sum_{ij\in\beta}(v^{\mathrm{H}}_{ijk\ell} - v^{\mathrm{F}}_{ijk\ell})(B^{-1})_{ki}(B^{-1})_{\ell j}, \tag{A.63}$$

$$v^{\mathrm{H}}_{ijk\ell} = \langle\varphi_i\varphi_j|\hat{v}|\varphi_k\varphi_\ell\rangle, \tag{A.64}$$

$$= \langle\phi_i\phi_j|e^{-a\boldsymbol{r}^2}|\phi_k\phi_\ell\rangle\langle\chi_i\eta_\alpha\chi_j\eta_\beta|\hat{X}|\chi_k\eta_\alpha\chi_\ell\eta_\beta\rangle. \tag{A.65}$$

$$\langle\phi_i\phi_j|e^{-a\boldsymbol{r}^2}|\phi_k\phi_\ell\rangle = \int \mathrm{d}\boldsymbol{r}\mathrm{d}\boldsymbol{R}\, \phi_i^*(\boldsymbol{r}_1)\phi_j^*(\boldsymbol{r}_2)\phi_k(\boldsymbol{r}_1)\phi_\ell(\boldsymbol{r}_2), \tag{A.66}$$

$$= D_{ik}D_{j\ell}\int \mathrm{d}\boldsymbol{r}\, \prod_\sigma \left(\tfrac{\nu_\sigma}{\pi}\right)^{1/2} e^{-\nu_\sigma\left(r_\sigma-\frac{1}{2}Z^{(-)}_{ijk\ell,\sigma}\right)^2}, \tag{A.67}$$

$$= \boxed{D_{ik}D_{j\ell}\prod_\sigma(1-\lambda_\sigma)^{1/2}\exp\left(-\frac{1}{4}\lambda_\sigma\nu_\sigma Z^{(-)2}_{ijk\ell,\sigma}\right)}, \tag{A.68}$$

where $\lambda_\sigma \equiv a/(a+\nu_\sigma)$.

◦ *Coulomb potential*

The Coulomb potential is written as,

$$\frac{1}{|\boldsymbol{r}_i - \boldsymbol{r}_j|} = \frac{1}{r} = \frac{2}{\sqrt{\pi}}\int_0^\infty \mathrm{d}\xi\, e^{-r^2\xi^2}. \tag{A.69}$$

Thus, the kernel is expressed as,

$$\langle\phi_i\phi_j|\tfrac{1}{r}|\phi_k\phi_\ell\rangle = \frac{2}{\sqrt{\pi}}\int_0^\infty \mathrm{d}\xi\, \langle\phi_i\phi_j|e^{-\xi^2 r^2}|\phi_k\phi_\ell\rangle. \tag{A.70}$$

In practical calculation, the Coulomb interaction is approximated by a sum of seven Gaussians to reduce the computational cost:

$$\frac{1}{r} = \sum_{n=1}^{7} c_n \sqrt{\bar{\nu}} \exp\left\{ -(\nu_x \nu_y \nu_z)^{1/3} \left(\frac{r}{\gamma_n} \right)^2 \right\}, \tag{A.71}$$

where the dimensionless parameters c_n and n are listed in Tab. 7. The parameters are determined to yield approximate values of the Coulomb interaction when the matrix elements of Eq. (A.71) are calculated from the nucleon Gaussian wave packets.

Tab. 7 Dimensionless parameters for an approximation of the Coulomb interaction.

n	c_n	γ_n
1	0.437686	8.888000
2	-0.421877	6.244998
3	0.363035	4.358899
4	0.082946	3.000000
5	0.179389	2.000000
6	0.717984	1.224745
7	2.108150	0.500000

A.3 General expression of deformed Gaussian

In general, Eq. (2.3) can be extended to,

$$\phi_i(\boldsymbol{r}) = \left(\frac{|2M|}{\pi^3} \right)^{1/4} \exp\left\{ -{}^t(\boldsymbol{r} - \boldsymbol{Z}_i) M (\boldsymbol{r} - \boldsymbol{Z}_i) \right\}^2, \tag{A.72}$$

$$M = \begin{pmatrix} \nu_{xx} & \nu_{xy} & \nu_{xz} \\ \nu_{xy} & \nu_{yy} & \nu_{yz} \\ \nu_{xz} & \nu_{yz} & \nu_{zz} \end{pmatrix}. \tag{A.73}$$

under the assumption that M is a symmetric matrix: ${}^tM = M$, which reads to ${}^t\boldsymbol{r} M \boldsymbol{Z} = {}^t\boldsymbol{Z} M \boldsymbol{r}$ for example. Here, I only show the overlap calculated by Eq. (A.72) with different matrices M_1 and M_2.

$$- {}^t(\boldsymbol{r} - \boldsymbol{Z}_i^*) M_1 (\boldsymbol{r} - \boldsymbol{Z}_i^*) - {}^t(\boldsymbol{r} - \boldsymbol{Z}_k) M_2 (\boldsymbol{r} - \boldsymbol{Z}_k), \tag{A.74}$$

$$\begin{aligned} = &- {}^t\boldsymbol{r}(M_1 + M_2)\boldsymbol{r} + {}^t\boldsymbol{r}(M_1 \boldsymbol{Z}_i^* + M_2 \boldsymbol{Z}_k) + ({}^t\boldsymbol{Z}_i^* M_1 + {}^t\boldsymbol{Z}_k M_2)\boldsymbol{r} \\ &- {}^t\boldsymbol{Z}_i^* M_1 \boldsymbol{Z}_i^* - {}^t\boldsymbol{Z}_k M_2 \boldsymbol{Z}_k. \end{aligned} \tag{A.75}$$

The first to third terms can be transformed as,

$$-{}^t\boldsymbol{r}M_{12}\boldsymbol{r}+{}^t\boldsymbol{r}M_{12}M_{12}^{-1}(M_1\boldsymbol{Z}_i^*+M_2\boldsymbol{Z}_k)+{}^t(M_1\boldsymbol{Z}_i^*+M_2\boldsymbol{Z}_k)M_{12}^{-1}M_{12}\boldsymbol{r}, \quad \text{(A.76)}$$

$$=-{}^t(\boldsymbol{r}-\widetilde{\boldsymbol{Z}})M_{12}(\boldsymbol{r}-\widetilde{\boldsymbol{Z}})+{}^t\widetilde{\boldsymbol{Z}}M_{12}\widetilde{\boldsymbol{Z}}, \quad M_{12}=M_1+M_2, \quad \text{(A.77)}$$

where $\widetilde{\boldsymbol{Z}}\equiv M_{12}^{-1}(M_1\boldsymbol{Z}_i^*+M_2\boldsymbol{Z}_k)$. Using the relation,

$$\widetilde{M}_{12}\equiv M_1M_{12}^{-1}M_2, \quad \text{(A.78)}$$

$$=M_1M_{12}^{-1}(M_1+M_2)-M_1M_{12}^{-1}M_1=(M_1+M_2)M_{12}^{-1}M_1-M_1M_{12}^{-1}M_1, \quad \text{(A.79)}$$

$$=M_2M_{12}^{-1}M_1=\widetilde{M}_{21}, \quad \text{(A.80)}$$

one can obtain equality:

$${}^t\widetilde{\boldsymbol{Z}}M_{12}\widetilde{\boldsymbol{Z}}-{}^t\boldsymbol{Z}_i^*M_1\boldsymbol{Z}_i^*-{}^t\boldsymbol{Z}_kM_2\boldsymbol{Z}_k=-{}^t(\boldsymbol{Z}_i^*-\boldsymbol{Z}_k)\widetilde{M}_{12}(\boldsymbol{Z}_i^*-\boldsymbol{Z}_k). \quad \text{(A.81)}$$

The overlap is calculated as,

$$\int \mathrm{d}\boldsymbol{r}\ \exp\{-{}^t(\boldsymbol{r}-\widetilde{\boldsymbol{Z}})M_{12}(\boldsymbol{r}-\widetilde{\boldsymbol{Z}})\}=\int \mathrm{d}\boldsymbol{R}\ \frac{\partial \boldsymbol{r}}{\partial \boldsymbol{R}}e^{-\boldsymbol{R}^2}=\pi^{3/2}|M_{12}|^{-1/2}, \quad \text{(A.82)}$$

where $\boldsymbol{R}=M_{12}^{1/2}(\boldsymbol{r}-\widetilde{\boldsymbol{Z}})$.

$$\therefore D_{ij}\equiv\langle\phi_i|\phi_j\rangle=\int \mathrm{d}\boldsymbol{r}\ \phi_i^*(\boldsymbol{r})\phi_j(\boldsymbol{r})=\boxed{\exp\left\{-{}^t(\boldsymbol{Z}_i^*-\boldsymbol{Z}_k)\widetilde{M}_{12}(\boldsymbol{Z}_i^*-\boldsymbol{Z}_k)\right\}}. \quad \text{(A.83)}$$

A.4 $N\alpha$ model of AMD wave function

In the self-conjugate nuclei, α cluster structures often emerge in the excited states. Therefore, $N\alpha$ model helps to understand the properties of the excited states. An α particle can be approximately described by the spin-fixed wave functions with spherical packet widths located at the same position $\boldsymbol{Z}$:

$$\Phi_\alpha(\boldsymbol{Z})=\mathcal{A}\{\phi(\boldsymbol{r}_1;\boldsymbol{Z})\chi_\mathrm{p}\eta_\uparrow\ \phi(\boldsymbol{r}_2;\boldsymbol{Z})\chi_\mathrm{p}\eta_\downarrow\ \phi(\boldsymbol{r}_3;\boldsymbol{Z})\chi_\mathrm{n}\eta_\uparrow\ \phi(\boldsymbol{r}_4;\boldsymbol{Z})\chi_\mathrm{n}\eta_\downarrow\}, \quad \text{(A.84)}$$

$$\nu_x=\nu_y=\nu_z. \quad \text{(A.85)}$$

This $N\alpha$ wave function was combined with the time-dependent variational principle and has applied for ^{12}C and ^{16}O [59, 60].

A.5 Laplace expansion of the AMD wave function

The Laplace expansion is a generalization of the cofactor expansion and is given for the determinant of an $A\times A$ matrix B as,

$$\big|B\big|=\sum_{1\le i_1\le\cdots<i_{C_1}\le A}P(i_1,\cdots,i_{C_1})\big|B(i_1,\cdots,i_{C_1})\big|\big|B(i_{C_1+1},\cdots,i_A)\big|, \quad \text{(A.86)}$$

$$\left|B(i_1,\cdots,i_{C_1})\right| = \begin{vmatrix} B_{1i_1} & \cdots & B_{1i_{C_1}} \\ \vdots & \ddots & \vdots \\ B_{C_1 i_1} & \cdots & B_{C_1 i_{C_1}} \end{vmatrix}, \tag{A.87}$$

$$\left|B(i_{C_1+1},\cdots,i_A)\right| = \begin{vmatrix} B_{C_1+1,i_{C_1+1}} & \cdots & B_{C_1+1,i_A} \\ \vdots & \ddots & \vdots \\ B_{A,i_{C_1+1}} & \cdots & B_{A,i_A} \end{vmatrix}, \tag{A.88}$$

where the summation runs over all possible combinations of indices $i_1 \leq \cdots < i_{C_1}$. The sign is expressed as,

$$P(i_1,\cdots,i_{C_1}) = \begin{pmatrix} 1 & \cdots & C_1 & C_1+1 & \cdots & A \\ i_1 & \cdots & i_{C_1} & i_{C_1+1} & \cdots & i_A \end{pmatrix} = (-)^{\frac{C_1(C_1+1)}{2}+\sum_{s=1}^{C_1} i_s}. \tag{A.89}$$

The A-body AMD wave function $\Phi^A_{\rm AMD}$ Eq. (2.3) can be decomposed into $\Phi^{C_1}_{\rm AMD}$ and $\Phi^{C_2}_{\rm AMD}$ by applying the Laplace expansion:

$$\Phi^A_{\rm AMD} = \sqrt{\tfrac{C_1!C_2!}{A!}} \sum_{1\leq i_1\leq\cdots<i_{C_1}\leq A} P(i_1,\cdots,i_{C_1})\Phi^{C_1}_{\rm AMD}(i_1,\cdots,i_{C1})\Phi^{C_2}_{\rm AMD}(i_{C_1+1},\cdots,i_A). \tag{A.90}$$

Appendix B Others

B.6 Charge radius $\sqrt{\langle r_c^2 \rangle}$

The mean-square charge radius $\langle r_c^2 \rangle$ is extrapolated from the point-proton radius of a nucleus $\langle r_p^2 \rangle$,

$$\langle r_c^2 \rangle = \langle r_p^2 \rangle + \left(R_p^2 + \frac{3\hbar}{(2M_p c)^2} \right) + \frac{N}{Z} R_n^2 + \langle r_{\rm so}^2 \rangle + \langle r_{\rm mec}^2 \rangle, \tag{B.91}$$

where R_p and R_n mean the proton and neutron charge radius, respectively. $\langle r_{\rm so}^2 \rangle$ and $\langle r_{\rm mec}^2 \rangle$ represent the spin-orbit effect and the meson-exchange currents, respectively. Eq. (B.91) corresponds to Eq. (6.48) in Ref. [61]. $R_p = 0.8775$ fm, $R_n = -0.1161$ fm, and $3\hbar/(2M_p c)^2 = 0.033$ fm^2 are applied.

B.7 Description of ^{11}Li wave function

I have artificially made the model wave function of ^{11}Li to reproduce the halo structure. Figure B.1 shows the energies for 0p0h-like and 2p2h-like before projected model wave functions of ^{11}Li as a function of the quadrupole deformation parameter β. The filled points of 0p0h and 2p2h wave functions are used for describing the proton and neutron parts of ^{11}Li, respectively, to reproduce the mixing of $(1s)^2$ and $(0d)^2$ configurations suggested in the previous studies,

$$\Phi_{\rm int} = \mathcal{A}\{\phi_{\rm p1}^{(0{\rm p}0{\rm h})} \cdots \phi_{\rm p3}^{(0{\rm p}0{\rm h})} \phi_{\rm n1}^{(2{\rm p}2{\rm h})} \cdots \phi_{\rm n8}^{(2{\rm p}2{\rm h})}\} \tag{B.92}$$

where the center of the system is shifted to be 0 (c.f. Eq.(2.4)).

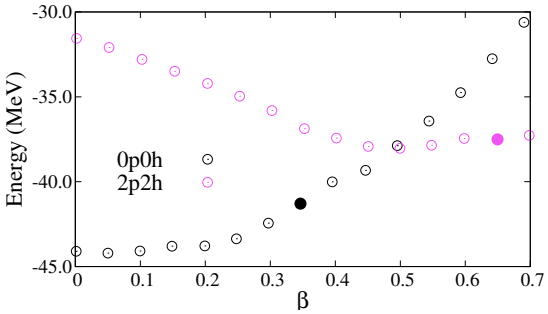

Fig. B.1 Energies for 0p0h-like and 2p2h-like before projected model wave functions of ^{11}Li as a function of the quadrupole deformation parameter β.

Acknowledgments

I appreciate Prof. Kimura, Prof. Zhou, Prof. Horiuchi, Prof. Aikawa, and Prof. Hirabayashi for their very kind advice and encouragement. I would like to thank the members of the nuclear theoretical group at Hokkaido University, especially H. Moriya and S. Shin, for their warm encouragement. This work was supported by JST SPRING, Grant Number JPMJSP2119.

References

[1] H. Motoki, Y. Suzuki, T. Kawai, and M. Kimura, Progress of Theoretical and Experimental Physics **2022**(11), 113D01 (2022).
[2] H. A. Bethe and R. F. Bacher, Rev. Mod. Phys. **8**, 82–229 (1936).
[3] J. A. Wheeler, Phys. Rev. **52**, 1107–1122 (1937).
[4] K. Ikeda, N. Takigawa, and H. Horiuchi, Progress of Theoretical Physics Supplement **E68**, 464–475 (1968).
[5] W. von Oertzen, M. Freer, and Y. Kanada-En' yo, Physics Reports **432**(2), 43–113 (2006).
[6] M. Seya, M. Kohno, and S. Nagata, Progress of Theoretical Physics **65**(1), 204–223 (1981).
[7] W. v. Oertzen, Zeitschrift fuer Physik A. Hadrons and Nuclei **354**, 37–43 (1996).
[8] Y. Kanada-En'yo, H. Horiuchi, and A. Doté, Phys. Rev. C **60**, 064304 (1999).
[9] N. Itagaki and S. Okabe, Phys. Rev. C **61**, 044306 (2000).
[10] Y. Kanada-En'yo, Phys. Rev. C **91**, 014315 (2015).
[11] M. Kimura, T. Suhara, and Y. Kanada-En' yo, The European Physical Journal A **52**(12), 1–38 (2016).
[12] W. Nörtershäuser, D. Tiedemann, M. Žáková, Z. Andjelkovic, K. Blaum, M. L. Bissell, R. Cazan, G. W. F. Drake, C. Geppert, M. Kowalska, J. Krämer, A. Krieger, R. Neugart, R. Sánchez, F. Schmidt-Kaler, Z.-C. Yan, D. T. Yordanov, and C. Zimmermann, Phys. Rev. Lett. **102**, 062503 (2009).
[13] M. Žáková, Z. Andjelkovic, M. L. Bissell, K. Blaum, G. W. F. Drake, C. Geppert, M. Kowalska, J. Krämer, A. Krieger, M. Lochmann, T. Neff, R. Neugart, W. Nörtershäuser, R. Sánchez, F. Schmidt-Kaler, D. Tiedemann, Z.-C. Yan, D. T. Yordanov, and C. Zimmermann, Journal of Physics G: Nuclear and Particle Physics **37**(5), 055107 (2010).
[14] A. Krieger, K. Blaum, M. L. Bissell, N. Frömmgen, C. Geppert, M. Hammen, K. Kreim, M. Kowalska, J. Krämer, T. Neff, R. Neugart, G. Neyens, W. Nörtershäuser, C. Novotny, R. Sánchez, and D. T. Yordanov, Phys. Rev. Lett. **108**, 142501 (2012).
[15] M. Ito, N. Itagaki, H. Sakurai, and K. Ikeda, Phys. Rev. Lett. **100**, 182502 (2008).
[16] P. G. Roos, N. S. Chant, A. A. Cowley, D. A. Goldberg, H. D. Holmgren, and R. Woody, Phys. Rev. C **15**, 69–83 (1977).
[17] T. A. Carey, P. G. Roos, N. S. Chant, A. Nadasen, and H. L. Chen, Phys. Rev. C **29**, 1273–1288 (1984).
[18] K. Yoshida, Y. Chiba, M. Kimura, Y. Taniguchi, Y. Kanada-En'yo, and K. Ogata, Phys. Rev. C **100**, 044601 (2019).
[19] J. Tanaka, Z. Yang, S. Typel, S. Adachi, S. Bai, P. v. Beek, D. Beaumel, Y. Fujikawa, J. Han, S. Heil, S. Huang, A. Inoue, Y. Jiang, M. Knösel, N. Kobayashi, Y. Kubota,

W. Liu, J. Lou, Y. Maeda, Y. Matsuda, K. Miki, S. Nakamura, K. Ogata, V. Panin, H. Scheit, F. Schindler, P. Schrock, D. Symochko, A. Tamii, T. Uesaka, V. Wagner, K. Yoshida, J. Zenihiro, and T. Aumann, Science **371**(6526), 260–264 (2021).
[20] K. Yoshida and J. Tanaka, Phys. Rev. C **106**, 014621 (2022).
[21] T. Wakasa, K. Ogata, and T. Noro, Progress in Particle and Nuclear Physics **96**, 32–87 (2017).
[22] S. Typel, Phys. Rev. C **89**, 064321 (2014).
[23] Q. Zhao, Y. Suzuki, J. He, B. Zhou, and M. Kimura, The European Physical Journal A **57**(5), 1–7 (2021).
[24] H. Horiuchi, Y. Kanada-En'yo, and A. Ono, Zeitschrift für Physik A Hadrons and Nuclei **349**(3), 279–283 (1994).
[25] Y. Kanada-En'yo and H. Horiuchi, Phys. Rev. C **52**, 647–662 (1995).
[26] H. Horiuchi and Y. Kanada-En'yo, Nuclear Physics A **616**(1), 394–405 (1997).
[27] Y. Kanada-En'yo and H. Horiuchi, Progress of Theoretical Physics Supplement **142**, 205–263 (2001).
[28] J. Berger, M. Girod, and D. Gogny, Computer Physics Communications **63**(1), 365–374 (1991).
[29] M. Kimura, Phys. Rev. C **69**, 044319 (2004).
[30] Y. Kanada-En'yo and H. Horiuchi, Progress of Theoretical Physics **93**(1), 115–136 (1995).
[31] M. Kimura, R. Yoshida, and M. Isaka, Progress of Theoretical Physics **127**(2), 287–301 (2012).
[32] D. L. Hill and J. A. Wheeler, Phys. Rev. **89**, 1102–1145 (1953).
[33] Y. Chiba and M. Kimura, Progress of Theoretical and Experimental Physics **2017**(5), 053D01 (2017).
[34] J. J. Krauth, K. Schuhmann, M. A. Ahmed, F. D. Amaro, P. Amaro, F. Biraben, T.-L. Chen, D. S. Covita, A. J. Dax, M. Diepold, et al., Nature **589**(7843), 527–531 (2021).
[35] P. Mueller, I. A. Sulai, A. C. C. Villari, J. A. Alcántara-Núñez, R. Alves-Condé, K. Bailey, G. W. F. Drake, M. Dubois, C. Eléon, G. Gaubert, R. J. Holt, R. V. F. Janssens, N. Lecesne, Z.-T. Lu, T. P. O'Connor, M.-G. Saint-Laurent, J.-C. Thomas, and L.-B. Wang, Phys. Rev. Lett. **99**, 252501 (2007).
[36] M. Seya, M. Kohno, and S. Nagata, Progress of Theoretical Physics **65**(1), 204–223 (1981).
[37] M. Ito, K. Kato, and K. Ikeda, Physics Letters B **588**(1), 43–48 (2004).
[38] Y. Kanada-En'yo, M. Kimura, and A. Ono, Progress of Theoretical and Experimental Physics **2012**(1) (2012).
[39] Y. Abe, J. Hiura, and H. Tanaka, Progress of Theoretical Physics **49**(3), 800–824 (1973).
[40] H. Furutani, H. Kanada, T. Kaneko, S. Nagata, H. Nishioka, S. Okabe, S. Saito, T. Sakuda, and M. Seya, Progress of Theoretical Physics Supplement **68**, 193–302 (1980).
[41] Y. Kanada-En'yo, Phys. Rev. C **85**, 044320 (2012).
[42] K. Wildermuth and Y. C. Tang, *A Unified theory of the nucleus. [Monograph]*, (1977).
[43] H. Fortune and R. Sherr, The European Physical Journal A **48**(7), 1–5 (2012).
[44] N. Shulgina, B. Jonson, and M. Zhukov, Nuclear Physics A **825**(3), 175–199 (2009).
[45] C. De Jager, H. De Vries, and C. De Vries, Atomic Data and Nuclear Data Tables **14**(5), 479–508 (1974).
[46] R. Sánchez, W. Nörtershäuser, G. Ewald, D. Albers, J. Behr, P. Bricault, B. A. Bushaw, A. Dax, J. Dilling, M. Dombsky, G. W. F. Drake, S. Götte, R. Kirchner, H.-J. Kluge, T. Kühl, J. Lassen, C. D. P. Levy, M. R. Pearson, E. J. Prime, V. Ryjkov, A. Wojtaszek, Z.-C. Yan, and C. Zimmermann, Phys. Rev. Lett. **96**, 033002 (2006).
[47] N. Imai, N. Aoi, H. Ong, H. Sakurai, K. Demichi, H. Kawasaki, H. Baba, Z. Dombrádi,

Z. Elekes, N. Fukuda, Z. Fülöp, A. Gelberg, T. Gomi, H. Hasegawa, K. Ishikawa, M. Ishihara, H. Iwasaki, E. Kaneko, S. Kanno, T. Kishida, Y. Kondo, T. Kubo, K. Kurita, S. Michimasa, T. Minemura, M. Miura, T. Motobayashi, T. Nakamura, M. Notani, T. Ohnishi, A. Saito, S. Shimoura, T. Sugimoto, M. Suzuki, E. Takeshita, S. Takeuchi, M. Tamaki, H. Watanabe, and K. Yoneda, Physics Letters B **673**(3), 179–182 (2009).

[48] P. Arumugam, B. K. Sharma, S. K. Patra, and R. K. Gupta, Phys. Rev. C **71**, 064308 (2005).

[49] B. Barnett, W. Gyles, R. Johnson, K. Erdman, J. Johnstone, J. Kraushaar, S. Lepp, T. Masterson, E. Rost, D. Gill, A. Thomas, J. Alster, I. Navon, and R. Landau, Physics Letters B **97**(1), 45–49 (1980).

[50] A. Estradé, R. Kanungo, W. Horiuchi, F. Ameil, J. Atkinson, Y. Ayyad, D. Cortina-Gil, I. Dillmann, A. Evdokimov, F. Farinon, H. Geissel, G. Guastalla, R. Janik, M. Kimura, R. Knöbel, J. Kurcewicz, Y. A. Litvinov, M. Marta, M. Mostazo, I. Mukha, C. Nociforo, H. J. Ong, S. Pietri, A. Prochazka, C. Scheidenberger, B. Sitar, P. Strmen, Y. Suzuki, M. Takechi, J. Tanaka, I. Tanihata, S. Terashima, J. Vargas, H. Weick, and J. S. Winfield, Phys. Rev. Lett. **113**, 132501 (2014).

[51] J. Kelley, E. Kwan, J. Purcell, C. Sheu, and H. Weller, Nuclear Physics A **880**, 88–195 (2012).

[52] F. Ajzenberg-Selove, Nuclear Physics A **523**(1), 1–196 (1991).

[53] H. Okuno, K. Asahi, H. Ueno, H. Izumi, H. Sato, M. Adachi, T. Nakamura, T. Kubo, N. Inabe, A. Yoshida, N. Fukunishi, T. Shimoda, H. Miyatake, N. Takahashi, W.-D. Schmidt-Ott, and M. Ishihara, Physics Letters B **354**(1), 41–45 (1995).

[54] H. Ueno, K. Asahi, H. Izumi, K. Nagata, H. Ogawa, A. Yoshimi, H. Sato, M. Adachi, Y. Hori, K. Mochinaga, H. Okuno, N. Aoi, M. Ishihara, A. Yoshida, G. Liu, T. Kubo, N. Fukunishi, T. Shimoda, H. Miyatake, M. Sasaki, T. Shirakura, N. Takahashi, S. Mitsuoka, and W.-D. Schmidt-Ott, Phys. Rev. C **53**, 2142–2151 (1996).

[55] F. Ajzenberg-Selove, Nuclear Physics A **506**(1), 1–158 (1990).

[56] H. Izumi, K. Asahi, H. Ueno, H. Okuno, H. Sato, K. Nagata, Y. Hori, M. Adachi, N. Aoi, A. Yoshida, G. Liu, N. Fukunishi, and M. Ishihara, Physics Letters B **366**(1), 51–55 (1996).

[57] H. Ogawa, K. Asahi, K. Sakai, T. Suzuki, H. Izumi, H. Miyoshi, M. Nagakura, K. Yogo, A. Goto, T. Suga, T. Honda, H. Ueno, Y. X. Watanabe, K. Yoneda, A. Yoshimi, N. Fukuda, Y. Kobayashi, A. Yoshida, T. Kubo, M. Ishihara, N. Imai, N. Aoi, W.-D. Schmidt-Ott, G. Neyens, and S. Teughels, Phys. Rev. C **67**, 064308 (2003).

[58] N. Itagaki, T. Naito, and Y. Hirata, Phys. Rev. C **105**, 024304 (2022).

[59] R. Imai, T. Tada, and M. Kimura, Phys. Rev. C **99**, 064327 (2019).

[60] Motoki, Hideaki and Kimura, Masaaki, EPJ Web Conf. **260**, 11019 (2022).

[61] W. Nörtershäuser and C. Geppert, The Euroschool on Exotic Beams, Vol. IV pages 233–292 (2014).